


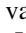










Characterization of High-priority Landing Sites for Robotic Exploration Missions in the Apollo Basin, Moon

Csilla Orgel^{1,2} , Ines Torres¹ , Sebastien Besse³ , Carolyn H. van der Bogert⁴ , Rickbir Bahia¹, René Prissang², Mikhail A. Ivanov⁵ , Harald Hiesinger⁴ , Gregory Michael², Jan Hendrik Pasckert⁴ , Mayssa El Yazidi⁶ , Balazs Bradak⁷ , and Sebastian H. G. Walter² 

¹ European Space Agency, European Space Research and Technology Centre (ESA/ESTEC), Directorate of Human and Robotic Exploration, Keplerlaan 1, 2201 AZ Noordwijk, The Netherlands

² Freie Universität Berlin, Institute of Geological Sciences, Planetary Sciences and Remote Sensing Group, D-12249 Berlin, Malteserstrasse 74-100, Bldg. D, Germany

³ European Space Agency, European Space Astronomy Centre (ESA/ESAC), Camino Bajo del Castillo s/n, Villanueva de la Canada, E-28692, Madrid, Spain

⁴ Universität Münster, Institut für Planetologie, D-48149 Münster, Wilhelm-Klemm-Str. 10, Münster, Germany

⁵ Vernadsky Institute, RAS, Russia

⁶ University of Maryland Global Campus, Building 126 Via Aldo Moro 80, I-36100 Vicenza, Italy

⁷ Laboratory of Exo-Oceans, Faculty of Oceanology, Kobe University, 5-1-1 Fukaeminami-machi, Higashinada-ku, Kobe 658-0022, Japan

Received 2023 August 29; revised 2023 November 22; accepted 2023 November 28; published 2024 February 2

Abstract

The South Pole–Aitken (SPA) basin is the oldest and largest visible impact structure on the Moon, making it a high priority science site for exploration missions. The 492 km diameter Apollo peak-ring basin is one of the youngest and largest basins within the SPA basin. We selected three regions of interest (ROIs) in the Apollo basin for which the landing and operational hazards are minimized and evaluated their science and in situ resource utilization (ISRU) potential. We examined topography, slope, crater density, rock abundance, geologic mapping, mineralogy, and inferred subsurface stratigraphy within each ROI. The results show that the terrain is safe for landing without precision landing (within a few hundred meters). The mare materials have high ISRU potential with relatively high FeO (~16–20 wt%) and TiO₂ (~3–10 wt%) contents. Two robotic exploration mission architectures were examined for their scientific potential: (1) lander and rover with a dedicated payload suite and (2) the same architecture with sample return capability. In situ observations can address six of seven National Research Council concepts (1–3, 5–7) and Campaigns 1 and 5 of the European Space Agency’s Strategy for Science at the Moon.

Unified Astronomy Thesaurus concepts: [The Moon \(1692\)](#); [Lunar science \(972\)](#)

1. Introduction

To date, there have been only five robotic rover missions to the lunar surface: Lunokhod-1 (roving distance: 9436 m; Karachevtseva et al. 2013), Lunokhod-2 (roving distance: 39,160 m; Karachevtseva et al. 2017), Chang’E-3/Yutu-1 (roving distance: 114 m; Qiao et al. 2015), Chang’E-4/Yutu-2 (ongoing roving distance: >1455 m as of 2023 January 26; Jones 2023), and Chandrayaan-3 (landed on 2023 August 23). The upcoming Chang’E-6 sample return mission is planned to land in the southern Apollo basin (e.g., Zeng et al. 2023).

As it is the oldest and largest visible impact structure on the Moon (Wilhelms et al. 1979, 1987; Garrick-Bethell & Zuber 2009; Smith et al. 2010; Garrick-Bethell et al. 2020), the South Pole–Aitken (SPA) basin, situated on the lunar farside, is a high-priority site for human and robotic exploration missions (Kring & Durda 2012; Jolliff et al. 2017; Allender et al. 2019; Jawin et al. 2019; Flahaut et al. 2020; Moriarty et al. 2021a; Jolliff et al. 2021; Keane et al. 2021; Lemelin et al. 2021; Cannon et al. 2023). Several national (e.g., NASA’s Artemis, Chang’E-6, and Chang’E-7), international (JAXA-ISRO Lunar Polar Exploration mission, ISRO Chandrayaan-3), and commercial lunar lander and sample return missions (e.g., NASA Commercial Lunar Payload Services missions, Ispace Hakuto-

R Mission 1 and Mission 2) will be directly or via the Lunar Gateway targeting the south polar region and SPA in the next decade.

Several mission concepts with 14 day durations are designed for short-distance (3.7 and 10.8 km), medium-distance (22.5 and 12.7 km), and long-distance (28.8 and 37 km) traverses of the Schrödinger basin (e.g., Potts et al. 2015; Steenstra et al. 2016; Allender et al. 2019, and additional references therein). More ambitiously, Steenstra et al. (2016) proposed a human-assisted robotic sample return mission concept in support of ESA’s HERACLES human-assisted sample return mission concept. This was based on a 3 yr mission plan where two robotic mission traverses are planned with an ESA-specified total traverse distance of 100–300 km.

On 2019 January 3, the Chinese Chang’E-4 mission became the first to land on the farside of the Moon, in Von Kármán crater (the northwest portion of the SPA) (Huang et al. 2018; Jia et al. 2018; Wu et al. 2019). Initially, the primary landing site for the Chang’E-4 robotic mission was the 492 km diameter Apollo basin (Figure 1), in the northeast quadrant of the SPA basin (Wang & Liu 2016), also a location of interest for NASA’s Constellation Program (Gruener & Joosten 2009). Additionally, the Endurance-R mission concept is targeting the Apollo basin with a rover traversing across the SPA basin interior from the Poincaré to the Apollo basin (Keane et al. 2021).

As the Apollo basin has remained a potential landing site for other future robotic, nonpolar exploration missions inside the SPA (Jawin et al. 2019), we studied the exploration potential of



Original content from this work may be used under the terms of the [Creative Commons Attribution 4.0 licence](#). Any further distribution of this work must maintain attribution to the author(s) and the title of the work, journal citation and DOI.

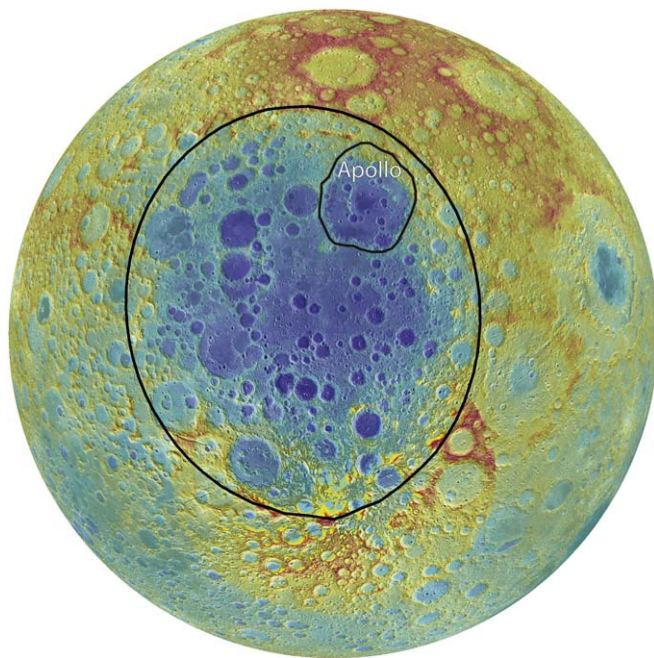


Figure 1. SPA (2400 × 2050 km) and Apollo (492 km) basins shown on the LOLA DEM 100 m pixel⁻¹ data (Smith et al. 2010) overlaid on LROC WAC (Robinson et al. 2010).

this basin, building on work done mapping this part of the SPA basin (Ivanov et al. 2018). We preselected three regions of interest (ROIs), located on both central and southern mare deposits, based on the inspection of terrain properties, hazards (e.g., varying topography and roughness, slopes, crater density, and rock abundance), scientific rationale, and high FeO and TiO₂ contents (Figures 2 and 3). Then, we performed a series of detailed geospatial and geostatistical analyses for each ROI using various optical, topographical, and spectral data sets in ArcGIS. Finally, we investigated how many key lunar science objectives of the US National Research Council (National Research Council 2007) and Campaigns 1 and 5 of the European Space Agency’s Strategy for Science at the Moon (European Space Agency 2019a) could be addressed and satisfied in such candidate landing sites in the Apollo basin.

Taking previous mission and concept studies into account, we chose exploration zones of similar size (2.5, 5, and 10 km) around each candidate landing site (e.g., Kring & Durda 2012; Karachevtseva et al. 2013; Potts et al. 2015; Qiao et al. 2015; Steenstra et al. 2016; Karachevtseva et al. 2017; Allender et al. 2019). We investigated the hazards, science, and in situ resource utilization (ISRU) potentials for a nominal mission phase using two robotic exploration mission scenarios: (1) lander and rover assets with a dedicated payload suite and (2) the same architecture with additional sample return capability. This paper is focused specifically on geoscience-related themes for landing site characterization.

2. Science Rationale: What Do We Know?

The SPA and Apollo basins exhibit a diverse suite of geological settings where numerous fundamental scientific questions can be addressed, which are summarized in Sections 2.1 and 2.2.

2.1. SPA Basin

The SPA basin is an elliptical-shaped giant impact structure, with a diameter of 2400 by 2050 km and a depth of approximately 13 km (Garrick-Bethell & Zuber 2009; Smith et al. 2010). Moreover, the SPA basin is the oldest observable impact structure on the Moon (4.26 ± 0.03 Gyr, Hiesinger et al. 2012; $4.31 +0.019/-0.021$ Gyr, Orgel et al. 2018).

Four distinct, approximately concentric mineralogical zones characterize the SPA basin (Lucey et al. 1998a; Jolliff et al. 2000; Pieters et al. 2001; Lawrence et al. 2002; Gibson & Jolliff 2011; Moriarty & Pieters 2018): (1) the SPA compositional anomaly in the SPA basin center, which exhibits Ca and Fe-rich pyroxenes; (2) an orthopyroxene annulus (OPX-A), dominated by Mg-rich pyroxenes; (3) a heterogeneous annulus (HET-A), which shows a mixture of Mg-rich pyroxenes and feldspathic materials; and (4) an SPA exterior with feldspathic composition (see Figure 9 of Moriarty & Pieters 2018). These mineralogical findings provide a framework for understanding of the formation, evolution, and subsequent geologic processes of the SPA basin and the early lunar crust and mantle.

As a consequence of such a large basin-forming impact event, the crustal thickness beneath SPA is less than 20 km, with local thicknesses of <5 km beneath the Apollo and Poincaré basins (Wieczorek et al. 2013). Additionally, the northwest of the SPA basin exhibits slightly enhanced thorium concentrations, while the floor of SPA is relatively low in thorium (Moriarty et al. 2021b). Thorium is a heat-producing element due to its radioactivity and could increase volcanic activity (Wieczorek & Phillips 2000). However, despite the thin crustal thickness, the presence of volcanic deposits across the SPA basin floor is minor compared to the nearside of the Moon (Yingst & Head 1999; Moriarty & Pieters 2015, 2016a; Whitten & Head 2015; Pasckert et al. 2018; Meyer et al. 2020; Chuang et al. 2022; Moriarty et al. 2022). There are several observations of pyroclastic deposits ranging from small (as in the Apollo basin and the center of the SPA basin) to large local deposits (as in the Oppenheimer crater and Schrödinger basin; Wilhelms et al. 1979; Gaddis et al. 2003; Borst et al. 2012; Kramer et al. 2013) and indicating a deeply seated mantle source around 400 km depths.

Moreover, other than the central peak/peak-ring structures of Schrödinger basin and Zeeman crater, a significant amount of olivine has not yet been detected within the SPA basin, the suggested main mineral phase of the lunar mantle that was expected to be exposed due to the SPA and subsequent basin-forming impact events (Yamamoto et al. 2012; Kramer et al. 2013). The absence of extensive olivine signatures suggests the presence of a mafic-rich primary crust or cumulate pile at the depth of excavation (Potter et al. 2018), which is in good agreement with the findings of Vaughan & Head (2014). Melosh et al. (2017) used three-dimensional numerical impact simulations and demonstrated that the SPA basin-forming event must have sampled the upper mantle to depths of 100 km. Observations from Moriarty et al. (2021b) show that the SPA impact melt is dominated by low-Ca pyroxene-dominated assemblages and suggest a stratified upper mantle at the time of the SPA formation.

2.2. Apollo Basin

The Apollo basin (36.09°S, 159.69°W) is the largest (492 km diameter; Baker et al. 2011) and one of the youngest well-

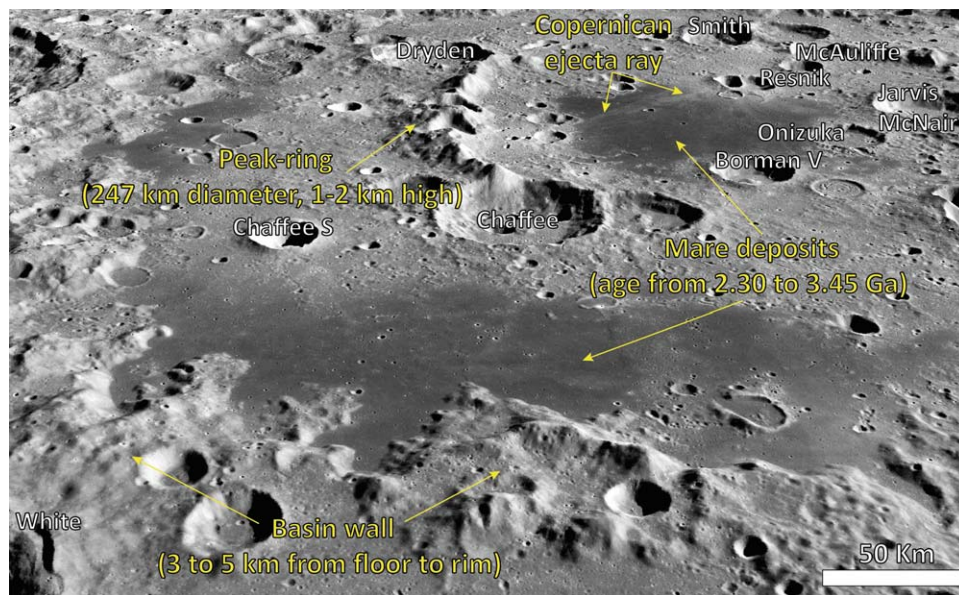


Figure 2. Oblique view of Apollo basin derived from a merged LRO LOLA and Kaguya TC 60 m pixel⁻¹ DEM (Barker et al. 2016) and 100 m pixel⁻¹ LROC WAC mosaic. Vertical exaggeration is 2×.

preserved peak-ring impact basins in the SPA basin ($3.91 \pm 0.04 / -0.06$ Gyr, Hiesinger et al. 2012; $3.98 \pm 0.04 / -0.06$ Gyr, Ivanov et al. 2018; $4.14 \pm 0.024 / -0.029$ Gyr, Orgel et al. 2018).

The inner peak ring has a diameter of 247 km and reaches heights of ~ 1 –2 km above the surrounding terrains (Baker et al. 2011). The inner peak-ring structure remained intact only in the west and northeast of the basin floor. The outer Apollo ring rises ~ 3 –5 km above the basin floor (Figures 2 and 3(a) and (b); Ivanov et al. 2018). The modeled crustal thickness beneath the Apollo basin is less than ~ 5 km, which is the thinnest in the entire SPA basin (Wieczorek et al. 2013). Baker & Head (2015) calculated a preimpact crustal thickness in the range of 27.0–35.3 km and a maximum depth of excavation of 39 km. Similarly, numerical modeling from Potter et al. (2018) gives estimates for preimpact crustal thickness in the range of 25–40 km and a depth of excavation of ~ 32 km.

From a mineralogical point of view, the Apollo basin overlays two mineralogical zones (Moriarty & Pieters 2018, their Figure 9): the HET-A and OPX-A terrains. Baker & Head (2015) defined the Apollo basin as the “Class C = $\leq 95\%$ plagioclase (+ pyroxene)” spectral type. However, they did not detect crystalline or shocked plagioclase on any outcrops. Furthermore, Potter et al. (2018) suggested that the absence of pure anorthosite is due to the magnitude of the impact, which shocked the crust and erased the $12.5 \mu\text{m}$ anorthosite band. However, the peak ring is dominated by pyroxenes (Klima et al. 2011; Moriarty & Pieters 2014; Baker & Head 2015), which might originate from the lower crust or could be explained by the presence of a differentiated SPA melt sheet (Hurwitz & Kring 2014; Vaughan & Head 2014). According to Melosh et al. (2017) and Moriarty et al. (2021b), the Apollo basin is located on the proximal ejecta blanket of the SPA basin, which had a thickness of up to 30 km; thus, it is unlikely that the SPA impact melt sheet extended out to the Apollo basin area. Moreover, the Th abundance maps show that the formation of the Apollo basin excavated entirely through the SPA ejecta blanket, exposing substrate crustal materials. Therefore, due to the deep excavation depths of both the SPA and Apollo basin-forming impacts and mineralogical

observations, the potential to find diverse rock types in the Apollo basin is high, which could allow us to better understand the internal structure and composition of the Moon.

The first geologic maps of the Apollo basin at 1:5M scale were compiled based on Apollo and Lunar Orbiter IV imagery by Stuart-Alexander (1978) and Wilhelms et al. (1979; Figure 3(e)). Recently, higher-resolution data sets from the Lunar Reconnaissance Orbiter Wide Angle Camera (LROC WAC) have allowed for the Apollo basin to be mapped at 1:500 K scale (Ivanov et al. 2018). It was found that two major classes of landforms are present: (1) impact craters and related features and (2) plains-forming terrains of volcanic (dark plains) and impact (light plains) origin (Wilhelms et al. 1979; Thiessen et al. 2012; Meyer et al. 2016; Ivanov et al. 2018; Pasckert et al. 2018; Meyer et al. 2020).

The basin floor is mainly covered by four major mare basalt provinces (Pasckert et al. 2018, their Figure 5) with absolute model ages (AMAs) ranging from 2.30 to 3.45 Gyr (central mare province: 2.93 Gyr, southern mare province: 3.31 and 3.45 Gyr; Pasckert et al. 2018) or from 2.44 Gyr (southern mare province) to 2.49/3.51 Gyr (central mare province; Haruyama et al. 2009). These mare deposits have enhanced FeO and TiO₂ contents, among the highest in the SPA basin, and are thus attractive for ISRU activities (Figures 3(f)–(h); Kring & Durda 2012; Pasckert et al. 2018). Additionally, Gaddis et al. (2003) described a small pyroclastic deposit (42 km^2) on the floor of a 20.5 km diameter crater on the outer ring of the Apollo basin. Based on low optical maturity and the lower returned Mini-RF radar signal and slightly lower FeO abundance than the average green glass composition of 19.5 wt% FeO, Trang et al. (2010) suggested that pyroclastics in the Apollo basin could be a new type of pyroclastic material.

Thiessen et al. (2012) mapped and derived AMAs from 3.4 to 3.8 Gyr for light plains deposits in the SPA, while Ivanov et al. (2018) report AMAs for three large fields of light plains in the northeast portion of SPA (outside of the Apollo basin) ranging from ~ 3.72 to ~ 3.80 Gyr. Moreover, Meyer et al. (2016, 2020) mapped the light plains deposits at 1:300K scale around the Orientale basin and globally, respectively, and

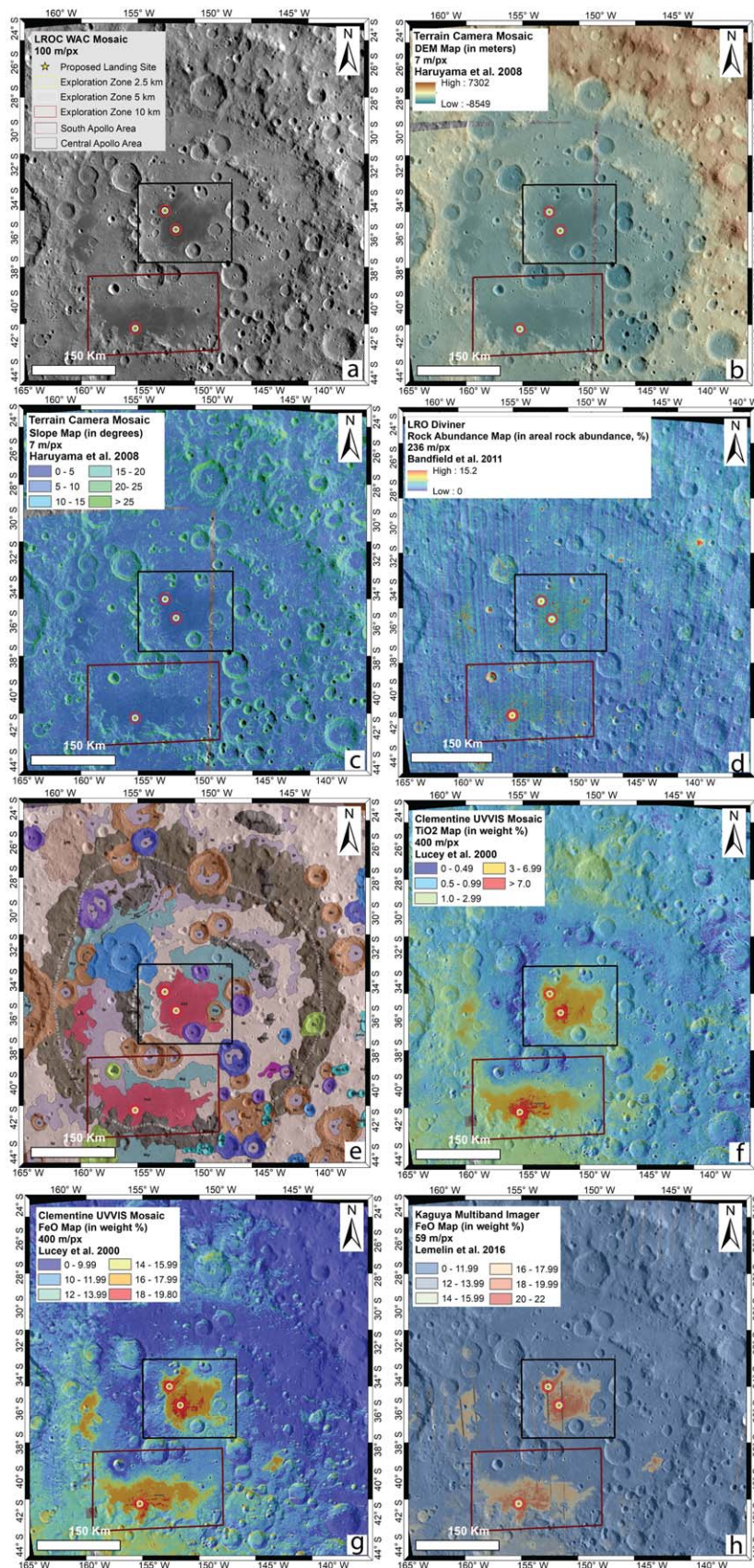


Figure 3. Maps of the Apollo basin overlaid on LROC WAC mosaic. (a) LROC WAC mosaic of 100 m pixel^{-1} , with three ROIs with a proposed central landing site (yellow star) and 2.5 (yellow), 5 (white), and 10 (red) km exploration zones. (b) Kaguya TC DEM (7 m pixel^{-1}). (c) Slope map derived from the Kaguya TC DEM. (d) Diviner Lunar Radiometer Experiment rock abundance map (236 m pixel^{-1}). (e) 1:5M scale unified geologic map of Fortezzo et al. (2020). (f) and (g) Clementine TiO₂ and FeO maps (400 m pixel^{-1} ; Lucey et al. 2000). ROIs overlap the highest FeO and TiO₂ concentrations. (h) Kaguya MI FeO map ($\sim 60\text{ m pixel}^{-1}$; Lemelin et al. 2016). All figures are in Lambert azimuthal equal-area projection, centered at -152.0°W , -35.8°S .

genetically linked 70% of all light plains, including those in the Apollo basin, to the Imbrium and Orientale basin-forming events.

3. Selection Criteria for ROIs

Typically, landing site assessments are based on criteria including (1) terrain properties (e.g., topography, roughness, slopes, crater density, and rock abundance), (2) landing precision and operations constraints, (3) scientific interest, and (4) ISRU potential, which has become one of the driving forces to return to the lunar surface.

In order to find the most suitable candidate landing sites for a future robotic mission in the Apollo basin (Figure 3(a)), we selected three ROIs on the central and southern mare deposits, where most of the following criteria were fulfilled (Figure 3): (1) flat, smooth terrain with relatively gentle slopes of $<7^\circ$; (2) relatively low crater density and (3) rock abundance; (4) scientific diversity; and (5) high FeO (>18 wt%) and TiO₂ (>5 wt%) contents for ISRU.

3.1. Terrain Properties

A relatively flat and smooth terrain (Figure 3(b)) is one of the main requirements for landing safety and the surface navigation and operation of a mobile asset. The distribution of slopes (Figure 3(c)) at baselines relevant to landing and operations safety (e.g., Luna-25, $<7^\circ$, Djachkova et al. 2017; Chang'E-3, $<7^\circ$, Wu et al. 2014) is a key element in landing site assessment; thus, we considered $<7^\circ$ slopes at a 7 m baseline. On a generally flat mare deposit, steep slopes ($>25^\circ$; Basilevsky et al. 2014) are mostly associated with fresh craters, as craters generally become shallower and slopes become gentler with time (Fassett 2016). Thus, we avoided large craters ($D > 2.5$ km) within a 10 km exploration zone from the proposed candidate landing sites. We set this threshold value based on the range of values from previous missions (e.g., Apollo landing sites, <1 km, and Chang'E'3, $<\sim 6.7$ km, Basilevsky et al. 2015; Chang'E'4, 3.6 km, Huang et al. 2018). Additionally, the crater rims and proximal ejecta of relatively fresh craters within ~ 1 – 1.5 crater radii are often characterized by higher rock abundances, which are challenging for the mobility of a rover (Figure 3(d)). In general, mare deposits are less rocky than highlands, typically $<0.5\%$, but fresh, small craters are typically “rocky” ($D >$ hundreds of m), showing more elevated rock concentrations with an areal fraction of less than 10% (Bandfield et al. 2011).

3.2. Landing Precision and Operations Constraints

The landing precision of a landing system and the resulting uncertainties on the exact landing point could influence the fulfillment of the science and ISRU objectives of a mission. Some of those objectives, e.g., finding water ice in localized areas, could require a landing system with capabilities for landing within hundreds of meters, while other requirements, e.g., targeting mare deposits with high TiO₂ and FeO in tens of km-scale areas, will not need a precision landing. Thus, we do not consider landing precision and operations in our study.

3.3. Scientific Potential

These ROIs address several scientific objectives as outlined in various strategy documents, including the Lunar Exploration Roadmap developed by the Lunar Exploration Analysis Group (Lunar Exploration Analysis Group 2016a), the Advancing Science of the Moon: Report of the Specific Action Team released by the Lunar Exploration Analysis Group (2017), the Lunar Science for Landed Missions Workshop Findings Report (Jawin et al. 2019) built upon the US National Research Council (National Research Council 2007) report, and Crawford et al. (2012), which provide guidelines for the scientific challenges and opportunities enabled by robotic and human exploration of the Moon. Based on the scientific potential of the Apollo basin, we selected three ROIs that provide a diverse geologic history and a variety of rock types (Figure 3(e)), which could be potentially visited by a well-equipped lander and rover within a 10 km exploration zone.

The National Research Council (2007) report prioritizes eight science concepts and goals for lunar exploration. In this study, we consider concepts 1–7 as we focus on addressing lunar surface and interior goals (concept 8 addresses the lunar exosphere). We summarize the National Research Council (2007) concepts and goals, Campaigns 1 and 5 of the European Space Agency’s Strategy for Science at the Moon (European Space Agency 2019a), and Strategic Knowledge Gaps (Lunar Exploration Analysis Group 2016b) relevant for the ROIs in Table 1 and Figures 15 and 16.

3.4. ISRU Potential

Robotic missions will target landing sites with high ISRU potential to allow the characterization of volatiles (e.g., H₂O) and mineral resources (e.g., ilmenite, FeTiO₃) that can be extracted from the regolith and utilized to produce fuel, oxygen, and building materials via ISRU (e.g., Allen et al. 2012; Allen 2015; Ehresmann et al. 2017; van der Bogert et al. 2021). Theme 1 of NASA’s Strategic Knowledge Gaps (SKG) summarizes the gaps in exploration science, technology development, and necessary measurements needed to close ISRU-related gaps in knowledge (Lunar Exploration Analysis Group 2016b; Table 1). One of the priority areas for the space resources activities of the ESA Space Resources Strategy (European Space Agency 2019b) is to establish the resource potential of regolith and pyroclastic deposits across the lunar surface by the identification and characterization of at least one nonpolar deposit. These goals are being pursued through a commercial ISRU technology development program (e.g., van der Bogert et al. 2021). To allow the characterization of mare basalt regolith for potential ISRU, we preselected ROIs where the highest FeO and TiO₂ values occur in the Apollo basin.

4. Data and Methods

4.1. Data

To evaluate the potential scientific return of each proposed ROI, we used available data sets from previous lunar missions, such as the Lunar Reconnaissance Orbiter (LRO), Kaguya, Clementine, Chandrayaan-1, and mission concept studies (Kring & Durda 2012); these data sets were integrated in ArcGIS 10.7 and projected in the Lambert azimuthal equal-area projection, centered at -152.0°W , -35.8°S .

Table 1
Summary of Lunar Geoscience and ISRU Knowledge Gaps

National Research Council (2007)	<ol style="list-style-type: none"> 1. The bombardment history of the inner solar system is uniquely revealed on the Moon. 2. The structure and composition of the lunar interior provide fundamental information on the evolution of a differentiated planetary body. 3. Key planetary processes are manifested in the diversity of lunar crustal rocks. 4. Lunar volatiles increase our understanding of the composition state and distribution of volatiles in the lunar polar regions. 5. Lunar volcanism provides a window into the thermal and compositional evolution of the Moon. 6. The Moon is an accessible laboratory for studying the impact process on planetary scales. 7. The Moon is a natural laboratory for regolith processes and weathering on anhydrous airless bodies.
European Space Agency’s Strategy for Science at the Moon (European Space Agency 2019a)	Campaign 1: analysis of new lunar samples
NASA’s SKG related to ISRU (Lunar Exploration Analysis Group 2016b)	Campaign 5: near-surface geology, geophysics, mineralogy, and geochemistry Theme 1C/regolith 2: quality/quantity/distribution/form of H species and other volatiles in nonpolar mare and highlands regolith Theme 1G/lunar ISRU production efficiency 2: measure the actual efficiency of ISRU processes in the lunar environment using technology (e.g., produce and store small quantities of hydrogen and oxygen from lunar regolith, demonstrate disposal of heated regolith after processing, process at high temperature to test techniques for extracting metals (e.g., Fe, Al) from regolith)

The terrains that compose the Apollo basin are visualized using an LROC WAC global mosaic (100 m pixel⁻¹; Robinson et al. 2010), a Kaguya Terrain Camera (TC) orthomosaic (7 m pixel⁻¹; Kato et al. 2010), and individual LROC Narrow Angle Camera (NAC) images (~1 m pixel⁻¹; Robinson et al. 2010). We used the Kaguya TC images as the photobase for geologic mapping at a scale of 1:50,000 for the central and southern portions of the Apollo basin, thus providing a higher-resolution geologic map than those of Ivanov et al. (2018) and Poehler et al. (2021). Then, to derive crater densities, we mapped craters >70 m in diameter (resolvable within 10 pixels or more in Kaguya TC) in various degradation states (Wu et al. 2014) across the selected areas.

Geologic mapping and terrain hazards were assessed via the merged LRO Lunar Orbiter Laser Altimeter (LOLA) and Kaguya TC Digital Elevation Model (DEM) global mosaic (60 m pixel⁻¹; Barker et al. 2016) and the Kaguya TC DEM global mosaic (7 m pixel⁻¹; Haruyama et al. 2008, 2012), respectively. Detailed slope maps were derived from the TC DEM by applying the Surface Slope tool in ArcMap. For both safety and scientific purposes, we used the LRO Diviner Lunar Radiometer Experiment 236 m pixel⁻¹ global rock abundance product. Rock abundance can be described in terms of the fraction of each pixel covered by exposed rocks (Bandfield et al. 2011). Numerous small young craters ($D >$ hundreds of m in diameter) expose abundant rocks on lunar maria, typically <0.5% rock concentration values. The distribution of “rocky craters” helps to identify hazards for landing and mobility of rovers on the lunar surface.

For assessing mare compositions and evaluating ISRU potential, we determined FeO and TiO₂ contents using both the Clementine Ultraviolet/Visible Spectrometer (UVVIS) ~400 m pixel⁻¹ global maps (Lucey et al. 1998b; Lucey et al. 2000) and Kaguya Multiband Imager (MI) ~60 m pixel⁻¹ global data (Lemelin et al. 2016) for comparison. To extract the minimum, maximum, and average FeO and TiO₂ abundances (wt%) from Clementine UVVIS and Kaguya MI global raster data sets, we generated 50 random measurement points within the 10 km exploration zone of each ROI.

To study the composition of the surface and subsurface, we analyze impact crater ejecta (Ohtake et al. 2013; Huang et al.

2018; Fu et al. 2020) using the Chandrayaan Moon Mineralogy Mapper (M³, global mode: 146–155 m pixel⁻¹; Pieters et al. 2009) and Kaguya MI global data set at 60 m pixel⁻¹ (Lemelin et al. 2016). Specifically, we used the M³ L2 calibrated data from the Planetary Data System (PDS) that are radiometrically (Green et al. 2011), geometrically (Boardman et al. 2011), photometrically (Besse et al. 2013), and thermally (Clark et al. 2011) corrected.

4.2. Methods

4.2.1. Regolith Thickness Estimation

We estimated the uppermost regolith layer thickness in the ROI using all LROC NAC images available up to 2018 February. The coverage was almost complete (see Figure 10), but a few images had poor data quality. Regolith thickness was derived using the method from Quaide & Oberbeck (1968). Small ($D <$ 250 m), relatively fresh concentric craters (CCs) are strongly affected by variations in target properties (porosity, rock strength, and layering), regolith protolith (Head & Wilson 2020), and impact velocity (e.g., van der Bogert et al. 2017). According to Quaide & Oberbeck (1968), CCs form when the impactor hits the lunar regolith–mare interface. We used the following equation:

$$\text{regolith thickness} = \left(k - \frac{D_f}{D_a} \right) D_a \tan(\alpha) / 2,$$

where k is an empirical constant (0.86), D_f is the diameter of the inner concentric ring, D_a is the outer rim-to-rim diameter of a crater, and $\tan(\alpha)$ is the corresponding slope of the inner walls of fresh craters ($31^\circ \pm 2^\circ$). To map CCs, we primarily considered NAC images with smaller incidence angles (<55°) because of the proper differentiation between the CCs and normal flat-floored craters (Fa et al. 2014), but we also used images with higher incidence angles to fill gaps in image coverage. The distribution of CCs is sparse in the ROI. We used the ordinary kriging geostatistical technique (Oliver & Webster 1990) to interpolate the obtained regolith thickness values from each measurement point at the distance of the half of the mean second-closest neighbor distance within the 10 km

exploration zone (Figure 10). The regolith thickness was estimated by measuring the inner and outer rim diameter of the small CCs after Quaide & Oberbeck (1968). However, based on their hydrocode simulations of CCs, Prieur et al. (2018) suggest that (1) smaller strength discontinuities, such as impact melt sheets within the regolith/target, and (2) low-impact velocities are sufficient to form CCs, so these features may not exclusively represent regolith thickness effects. Thus, the estimated regolith thicknesses should be taken with caution.

4.2.2. Mineralogy

To infer the local stratigraphy, we analyzed the mineralogy of materials exposed by impact crater ejecta on the mare floor and basin material based on the premise that smaller craters expose shallow stratigraphic units, while larger craters excavate deeper units (Figure 11). We developed a python algorithm that generated a red, green, and blue (RGB) color-composite mosaic of M³ data covering the Apollo basin (Torres et al. 2022). As M³ has a wide spectral range (430–3000 nm), it enabled the analysis of the 1 and 2 μm regions, which are relevant for detecting lunar mafic minerals and plagioclase (e.g., Moriarty & Pieters 2016b; Martinot et al. 2018). The developed algorithm first extracts the reflectance of each pixel at a given wavelength, then derives the absorption band depth of each pixel with the continuum removal method modified after Martinot et al. (2018)—a straight line between two tie points at 730 and 1620 nm was used to remove the continuum. Note that we used the simplified version of the Martinot et al. (2018) technique by fixing the tie points instead of searching for individual tie points pixel by pixel due to the limitations in the computation power. Finally, the algorithm derives the integrated band depth of the 1 μm (789–1308 nm) and 2 μm (1658–2498 nm) regions for each pixel. For the RGB color-composite mosaic of M³ data to be sensitive to mafic composition, we used the integrated band depth at 1 μm (red), integrated band depth at 2 μm (green), and reflectance at 1580 nm (blue; Besse et al. 2011). Consequently, the red and yellow colors are indicative of high-Ca pyroxenes (basaltic material), green suggests the presence of low-Ca pyroxenes (noritic material), and blue represents anorthositic or low-Fe-bearing materials. We can distinguish between old and freshly exposed mare, as well as feldspathic terrain materials (Figure 11(a)). We selected seven measurement points related to diverse geologic features (Figure 11(a)): (1) the central mare province; (2) a fresh crater rim; (3) an “island” (kipuka) within ROI 1; (4) the distal ejecta from an unnamed crater overlaying Resnik crater; (5) the inner crater wall of “Crater 1,” the largest impact crater on the central mare province; (6) the proximal ejecta from an unnamed crater overlaying Resnik crater; and (7) freshly exposed material by a cluster of small craters. Moreover, we compared the M³ spectra from seven key locations with olivine,⁸ augite,⁹ and pigeonite¹⁰ from the PDS spectral library (Figure 11(b)).

Additionally, we created a Kaguya MI RGB color composite using band 1 at 415 nm, band 2 at 750 nm, and band 4 at

950 nm. To obtain a color ratio map, we applied color ratios of R, 750/415 nm (1.797–1.925); G, 950/750 nm (0.877–1.034); and B, 415/750 nm (0.515–0.564) following the work of Huang et al. (2018). Stretch values are in brackets.

4.2.3. Relative Stratigraphy

We studied the relative stratigraphy within the ROIs with two different approaches. The local and regional stratigraphy can be examined via observations of compositional variations within all impact crater ejecta (not limited to CCs) located on the mare floor using the Chandrayaan M³ pyroxene map and Kaguya MI data sets. The diversity of mineralogical signatures could suggest chemical variations with depth. To estimate the minimum thickness of specific strata, we measured the diameter of the craters using NAC images and calculated the crater excavation depth (H_{exc}) using the equation from Huang et al. (2018) and Melosh (1989):

$$H_{exc} = 0.084D,$$

where H_{exc} is the maximum excavation depth and D is the final crater diameter. It is important to note that the lack of availability of a full range of crater sizes (from hundreds of meters to kilometers) limits our ability to document mineralogical variations with depth.

To establish a relative stratigraphy for the geological units within the overall region of the Apollo basin, we used AMA data of large impact craters from Ivanov et al. (2018) and Fortezzo et al. (2020), as well as light plains deposits from Thiessen et al. (2012) and Meyer et al. (2016, 2020). Additionally, we placed impact structures without currently measured AMAs based on their degradation state (Ivanov et al. 2018) in the stratigraphic column from the direct vicinity of the Apollo basin and its interior. Both kinds of stratigraphic analyses provide geological context for further studies, as well as mission planning and operations, in the Apollo basin.

5. Results

5.1. Terrain Hazards: Slopes, Craters, and Rock Abundance

The selection of landing sites for lunar missions takes into consideration several key factors, including hazard mitigation. In this case, all proposed landing sites are situated on top of mare deposits, which have relatively flat terrain, ensuring safe and stable landing conditions. Additionally, the crater densities and rock abundances in these regions are low, reducing the risk of potential hazards.

Slope analysis based on 7 m baseline Kaguya TC DEM data reveals that the slopes in the proposed landing areas generally do not exceed 5°, making them suitable for landing and subsequent operations, although a few fresh craters exhibit steeper slopes exceeding 25° (Figure 4).

Within the 10 km exploration zones surrounding the landing sites, the number of craters with diameters of 70 m or larger is estimated to be less than ~1000. The average crater diameter ranges from 128 m in ROI 1 to 150 m in ROI 3, as indicated in Table 2 and Figure 5. The largest crater diameters are: ROI 1 (588 m), ROI 2 (983 m), and ROI 3 (2.3 km). Furthermore, the depths of crater excavation vary, ranging from approximately 5.9 m for the lower limit of the considered crater diameter range up to 195 m at ROI 3 for the largest crater observed there (Table 2).

⁸ https://pds-spectlib.rsl.wustl.edu/measurement.aspx?lid=urn:nasa:pds:relab:data_reflectance:c1ag08

⁹ https://pds-spectlib.rsl.wustl.edu/measurement.aspx?lid=urn:nasa:pds:relab:data_reflectance:c1ag10

¹⁰ https://pds-spectlib.rsl.wustl.edu/measurement.aspx?lid=urn:nasa:pds:relab:data_reflectance:c1dd155

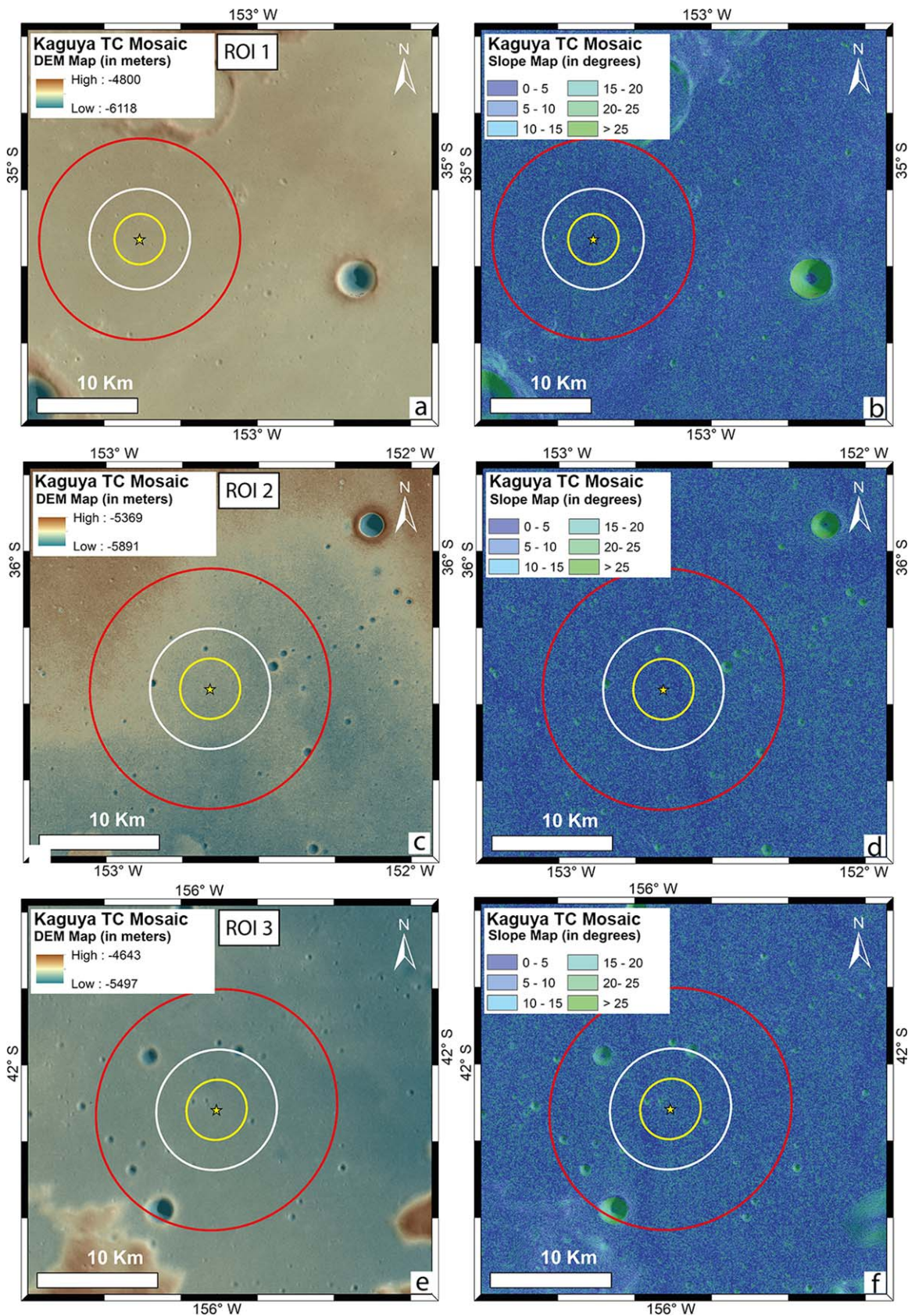


Figure 4. DEMs ((a), (c), and (e)) and slopes ((b), (d), and (f)) derived from the Kaguya TC 7 m pixel^{-1} stereo image mosaic for ROIs 1, 2, and 3, respectively. The circles indicate exploration zones of 2.5, 5, and 10 km from the proposed landing sites (yellow star). The maps are in Lambert azimuthal equal-area projection, centered at -152.0°W , -35.8°S .

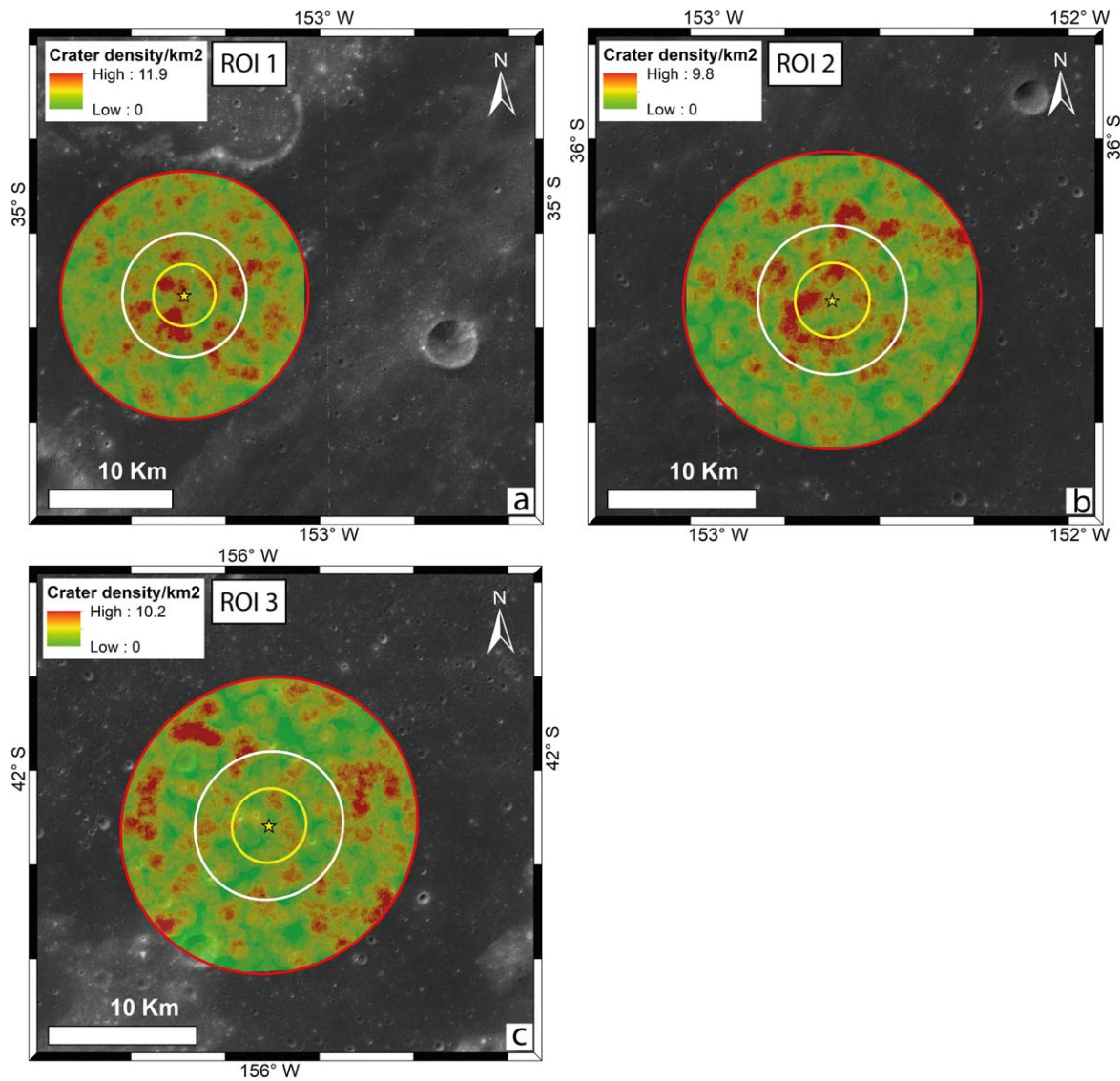


Figure 5. Maps of crater densities overlaid on the Kaguya TC 7 m pixel^{-1} mosaic on which craters $>70 \text{ m}$ in diameter were measured. (a) ROI 1, (b) ROI 2, and (c) ROI 3. The circles indicate exploration zones of 2.5, 5, and 10 km from the proposed landing sites (yellow star). The maps are in Lambert azimuthal equal-area projection, centered at -152.0°W , -35.8°S .

A relationship between crater age and boulder densities is observed, where younger craters tend to have higher boulder densities on their rims and within their proximal ejecta radial to the crater centers compared to older craters. In terms of areal rock density, ROI 1 exhibits the lowest value at 3.5%, while ROI 3 demonstrates the highest rock abundance at 14.1% within the 10 km exploration zone (Figure 6, Table 3).

These findings provide valuable insights for mission planning and resource assessment at the proposed landing sites. The relatively flat terrain, low crater densities, and rock abundances contribute to the favorable conditions for safe landing and operations.

5.2. Science Potential

5.2.1. Geologic Mapping of the Central and Southern Mare Provinces

The geologic mapping results correlate well with the geologic maps of Wilhelms et al. (1979), Ivanov et al. (2018), and Poehler et al. (2021), but this study generated

Table 2
Crater Statistics of Craters $>70 \text{ m}$ in Diameter within the Three ROIs

	ROI 1	ROI 2	ROI 3
Min. crater diameter (m)	70	70	70
Max. crater diameter (m)	588	983	2330
Average diameter (m)	128	138	150
Min. crater excavation depth (m)	5.9	5.9	5.9
Max. crater excavation depth (m)	49.5	82.6	196
Number of craters	966	767	739
Crater density km^{-2}	0–11.9	0–9.9	0–10.3

higher-resolution maps. Here, we identified three major classes of landforms that we mapped in the central and southern Apollo basin at 1:50,000 mapping scale (Figures 7 and 8). A correlation chart of the mapped geologic units is shown in Figure 9. The following geologic unit groups are defined in Ivanov et al. (2018) and Wilhelms et al. (1979) and used in our map as well.

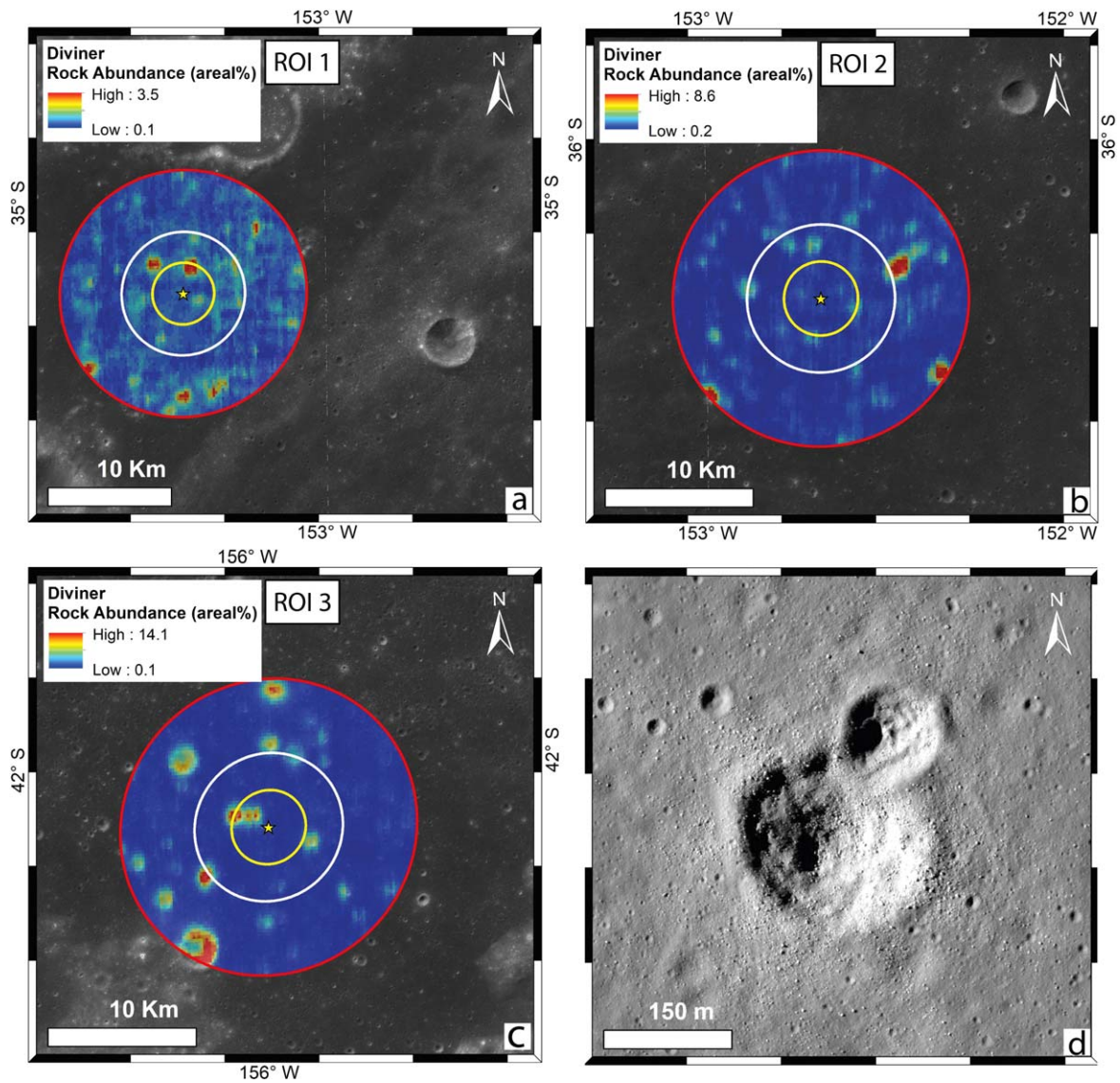


Figure 6. Rock abundance derived from LRO Diviner 236 m pixel⁻¹ data overlaid on the Kaguya TC mosaic (a), (b), and (c) for ROIs 1, 2, and 3, respectively. (d) Example of a “rocky” young crater. The circles indicate exploration zones of 2.5, 5, and 10 km from the proposed landing sites (yellow star). The maps are in Lambert azimuthal equal-area projection, centered at -152.0°W , -35.8°S .

1. Basin massif materials group.

- (a) Pre-Nectarian/Nectarian basin massif material unit (*NpNbm*): forms the inner peak-ring massif and outer-ring massif of the Apollo basin, originating from uplifted crustal material during basin formation.
- (b) Pre-Nectarian/Nectarian hummocky basin material unit (*NpNbh*): represents the residual impact melt of basin formation.

2. Plains-forming materials group.

- (a) Imbrian mare material unit (*Im*): dark albedo unit of volcanic origin.
- (b) Imbrian light plains material unit (*Ip*): light albedo, highly cratered unit, likely of impact ejecta origin, from remote craters and basins. This unit overlies various older geologic units and is preserved in low-topographic areas.

3. Impact crater materials group: stratigraphic age is based on the degradation state of the impact crater morphology after Wilhelms et al. (1987).

Table 3

Rock Abundance (in Areal %) Based on LRO Diviner 236 m pixel ⁻¹ Data			
	ROI 1	ROI 2	ROI 3
Min.	0.1	0.2	0.1
Max.	3.5	8.6	14.1

- (a) Copernican craters (*Cc*) have crisp, well-preserved impact morphologies with prominent ejecta rays and secondary craters and overlay or cut across all other geologic units.
- (b) Eratosthenian craters (*Ec*) have sharp-crested rim morphologies without prominent ejecta rays.
- (c) Imbrian craters (*Ik*) are well-preserved large craters with complex morphologies and subdued ejecta deposits.
- (d) Pre-Nectarian and Nectarian craters (*NpNc*) are heavily degraded large craters without obvious ejecta deposits.

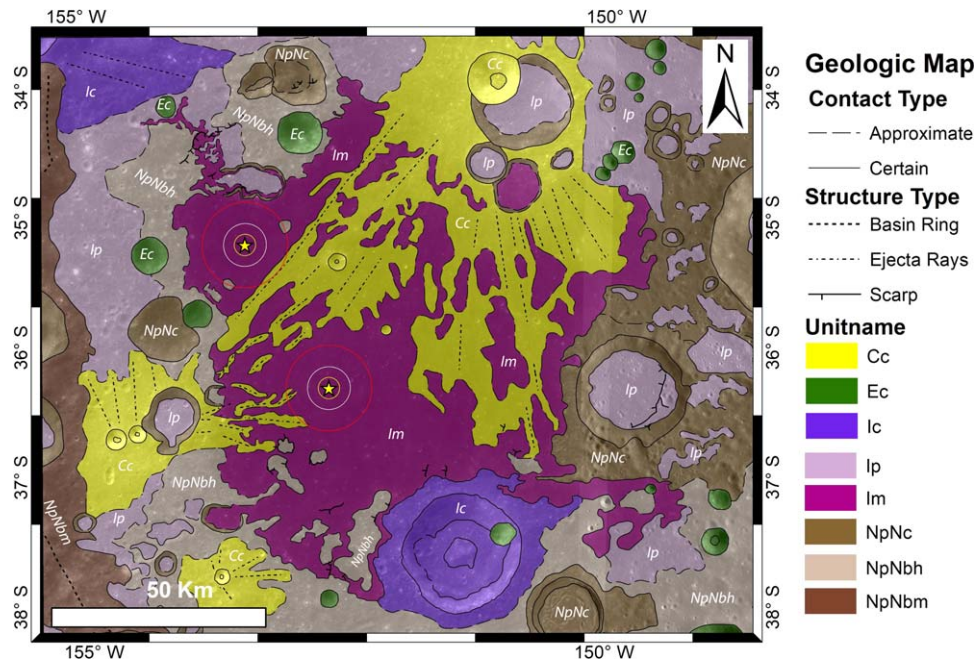


Figure 7. Geologic map of the central mare province of the Apollo basin overlaid on Kaguya TC and LROC WAC at 1:50,000 mapping scale. ROI 1 (upper) and ROI 2 (lower) are indicated with circular exploration zones of 2.5, 5, and 10 km from the proposed landing sites (yellow star). The maps are in Lambert azimuthal equal-area projection, centered at -152.0°W , -35.8°S .

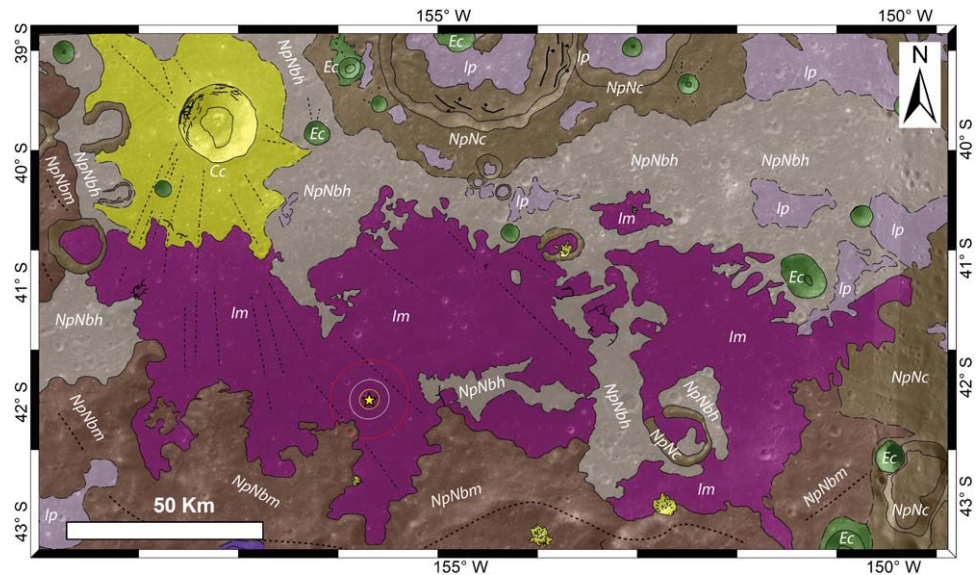


Figure 8. Geologic map of the southern mare province of the Apollo basin overlaid on Kaguya TC and LROC WAC at 1:50,000 mapping scale. ROI 3 is indicated with circular exploration zones of 2.5, 5, and 10 km from the proposed landing site (yellow star). Same legend as in Figure 7. The maps are in Lambert azimuthal equal-area projection, centered at -152.0°W , -35.8°S .

During the pre-Nectarian/Nectarian period, the Apollo basin formed in the northeastern section of the SPA basin rim (e.g., Ivanov et al. 2018) and on the proximal ejecta blanket of the transient crater cavity of the SPA basin (Melosh et al. 2017; Moriarty et al. 2021b). It is distinguished by its intricate peak-ring basin structure (*NpNbm*) and the presence of hummocky terrain (*NpNbh*). The hummocky terrain is interpreted by Ivanov et al. (2018) to be an impact melt located within the inner peak ring and between the inner peak ring and the outer ring. Subsequently, a series of craters (*NpNc*) formed in the area, such as Onizuka, Resnik, Jarvis, Oppenheimer, Chaffee, and Chawla craters. These craters have significantly altered the

landscape of the Apollo basin, and they typically exhibit extensive degradation and lack ejecta deposits.

During the Imbrian period, light plains deposits (*Ip*) were formed, originating from various older geological units and notably including material from the Orientale impact event, as suggested by Meyer et al. (2016, 2020). Ivanov et al. (2018) estimated AMAs for three large light plains deposits and concluded a range from ~ 3.80 to ~ 3.72 Gyr suggesting different sources of origin. These deposits are found overlaying other geological units and are primarily preserved in flat, low-lying areas. The surface of the light plains deposits exhibits a high density of impact craters and possesses a higher albedo

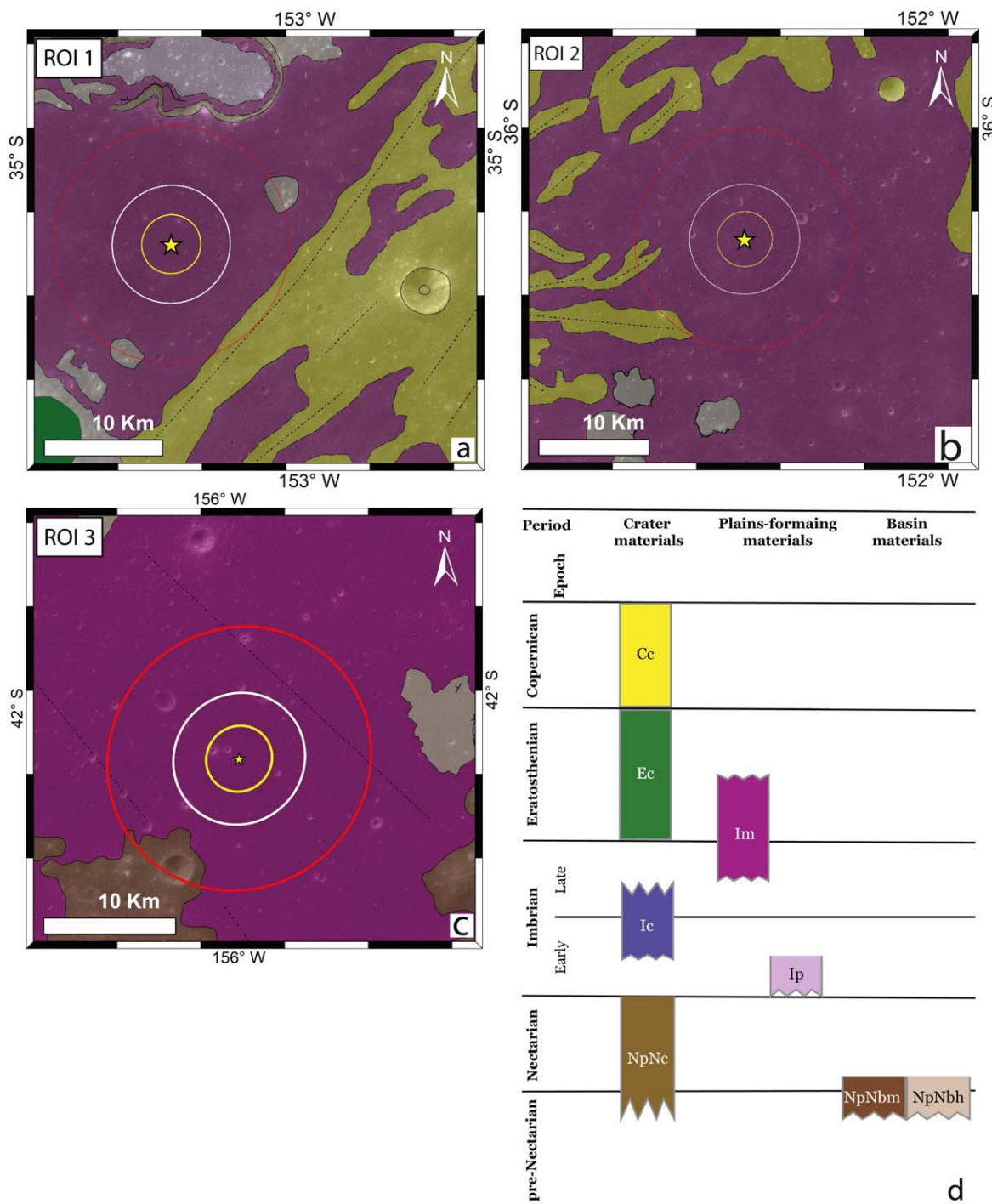


Figure 9. Geologic maps of ROIs overlaid on the Kaguya TC image, with exploration zones of 2.5, 5, and 10 km from the proposed sites (yellow star). (a) ROI 1 has access to study *Im*; Copernican-aged ejecta (*Cc*), which might excavate SPA and Apollo impact melt from the subsurface; and remnants of *NpNbh* with putative impact melt origin. (b) ROI 2 could sample different Copernican-aged ejecta rays (*Cc*), potential SPA and Apollo impact melt materials, and Imbrian mare deposit. (c) ROI 3 could investigate Imbrian mare deposits, as well as *NpNbm*. (d) Geologic correlation chart of geologic units. The maps are in Lambert azimuthal equal-area projection, centered at -152.0°W , -35.8°S .

compared to mare deposits. Following the formation of the *Ip* unit, the southern and central mare provinces (*Im*) were emplaced, as described by Haruyama et al. (2009) and Pasckert et al. (2018). Additionally, a large crater called Dryden crater (*Ic*), shown in Figure 2, is well preserved and displays complex morphology. Its ejecta deposit appears subdued and overlaps with pre-Nectarian/Nectarian craters. There are two possible explanations for this observation. One possibility is that the

ejecta deposit of Dryden crater has undergone significant degradation, making it difficult to establish a clear stratigraphic relationship with the surrounding mare deposit. Consequently, the stratigraphic relationship remains uncertain. Alternatively, Dryden crater could have formed before the mare flooded the central area of the Apollo basin. This hypothesis is supported by the absence of ejecta overlaying the central mare deposit and of excavated mare dykes/intrusions on Dryden’s crater wall

(Moriarty & Pieters 2014). Of the two hypotheses, the latter is favored due to the lack of visible ejecta over the central mare deposit. This suggests that Dryden crater predates the mare flooding in the central area of the Apollo basin.

The younger *Ec* exhibit distinct rim morphologies with sharp crests and lack prominent ejecta rays. In contrast, the youngest *Cc* display well-preserved impact features with crisp morphologies, prominent ejecta rays, and the presence of secondary craters (e.g., Wilhelms et al. 1979). These *Cc* are observed to overlay or cut across all other geologic units in the area. Both mare provinces are influenced by larger *Cc*. In the southern mare deposit, the ejecta from the Chaffee S crater, which is approximately 20 km in diameter and located in the northwest quadrant of the mapping area (Figure 8), affects the region. However, the ejecta deposit of the Chaffee S crater is poorly visible and presents challenges in confident mapping. Likewise, the central mare province is affected by an unnamed crater that has a well-preserved ejecta deposit overlaying Resnik crater (Figure 7). This distinct ejecta deposit can be traced back to the unnamed crater as its source. These observations provide insights into the impact history of the region, with the younger *Ec* and *Cc* exhibiting different morphological characteristics and affecting the geological units in distinctive ways.

In summary, ROI 1 offers a diverse range of geologic materials within the 10 km exploration zone, making it an intriguing area for a rover mission (Figure 9(a)). The region contains three distinct units: *Im*, *Cc*, and *NpNbh*. The *Im* unit represents the central mare province and is characterized by its formation during the Imbrian period. The *Cc* unit corresponds to the youngest Copernican craters, displaying well-preserved impact features with prominent ejecta rays and secondary craters. These craters have left their mark on the landscape, superposing other geological units. The *NpNbh* unit is particularly interesting. It is believed to have an impact melt origin and may contain materials derived from the SPA basin and the Apollo impact melt breccia, as suggested by Wilhelms et al. (1979) and Ivanov et al. (2018). However, other studies (e.g., Melosh et al. 2017; Moriarty et al. 2021b) suggest that there is no SPA material to be found in the Apollo basin. This unit forms isolated “islands” known as kipukas within the mare deposit, and two such kipukas are located within ROI 1. Additionally, it is possible that the *NpNbh* unit can be found within the ejecta deposit of the unnamed crater on top of Resnik crater, largely overlapping the central mare deposit and in part of ROI 1. The geologic diversity within ROI 1, encompassing *Im*, *Cc*, and the intriguing *NpNbh* unit, presents an exciting opportunity for scientific exploration and further understanding of the lunar geologic history.

ROI 2 is situated within the *Im* unit, specifically in an area where the ejecta deposits from various *Cc* merge, originating from both the northeast and southwest directions, particularly evident in the southwestern part of the 10 km exploration zone (Figure 9(b)). It is worth noting that these Copernican-aged ejecta deposits, similar to ROI 1, may have excavated the *NpNbh* unit, potentially exposing its material through the impact process.

ROI 3 is located within the *Im* unit, in close proximity to the outer ring of the Apollo basin, known as the *NpNbm* unit (Figure 9(c)). This location shares a similar geologic setting with the Apollo 17 landing site, which was situated in the Taurus–Littrow Valley on the eastern edge of Mare Serenitatis, surrounded by remnants of the Serenitatis basin massif.

Table 4

Regolith Thickness Estimated Using CCs and the Equation from Quaide & Oberbeck (1968)

	ROI 1	ROI 2	ROI 3
Min. (m)	1.1	1.2	1.2
Max. (m)	24	18.5	19.9
Average (m)	5.7	8.3	4.6
STDV	3.9	3.2	3.3

Note. It should be noted that the values could indicate only a minimum regolith thickness.

Compared to ROI 1 and ROI 2, ROI 3 exhibits less disturbance from reworked materials. This implies that a landing site in ROI 3 retains a more pristine and less altered geologic environment, making it an intriguing location for further exploration and study. The geologic similarity to the Apollo 17 landing site suggests that ROI 3 may offer valuable insights into the lunar geology and contribute to our understanding of the formation and evolution of the Apollo basin.

5.2.2. Regolith Thickness, Mineralogy, and Subsurface Stratigraphy

The lunar surface is predominantly covered by a layer of fine-grained regolith, which is the product of continuous impact processes. Our research has revealed that the average thickness of the regolith varies between 4.6 and 8.3 m, as shown in Table 4 and Figure 10. These findings align well with previous studies conducted by Quaide & Oberbeck (1968), Fa et al. (2014), Huang et al. (2018), and Fu et al. (2020).

Analysis of M³ data does not indicate the presence of distinct lava flows, suggesting that each mare province in the Apollo basin experienced a single magmatic event (Figure 11(a)). Alternatively, M³ data might only indicate distinct lava flows if they were substantially different in composition, as the data are affected by several artifacts (e.g., striping, image boundaries). Additionally, we have observed a lack of diversity in pyroxene mineralogy, which is in contrast to the variations in pyroxenes observed in the Von Karman crater due to exposure by small and large craters (Huang et al. 2018), which could be interpreted by significantly more mixing events from local crater ejecta blankets. Figure 11(a) illustrates a mature mare deposit (marked as number 1) characterized by red color. Small yellow craters (numbers 2 and 7) exhibit high-calcium clinopyroxene (HCP) mineralogy, representing fresh and immature basaltic material (number 5). The ejecta ray of an unnamed large Copernican-aged crater overlaying Resnik crater displays similar mineralogy to the *NpNbh* geologic unit, marked in blue (numbers 3, 4, and 6). These areas exhibit higher reflectance at 1580 nm, consistent with feldspathic material. The variations observed in the Kaguya RGB composite image demonstrate contrasts in titanium and iron contents, as well as surface maturity (Figure 11(c)). Larger craters, such as “Crater 1,” exhibit distinct composition and/or represent the illuminated crater walls and/or relatively “fresher” material (depicted in red). However, it is important to approach the interpretation of these results with caution due to the potential diversity in preimpact geology, including intrusions of different compositions. These variations could lead to erroneous interpretations compared to our current understanding of the structure of the lunar crust, as suggested by Martinot et al. (2018).

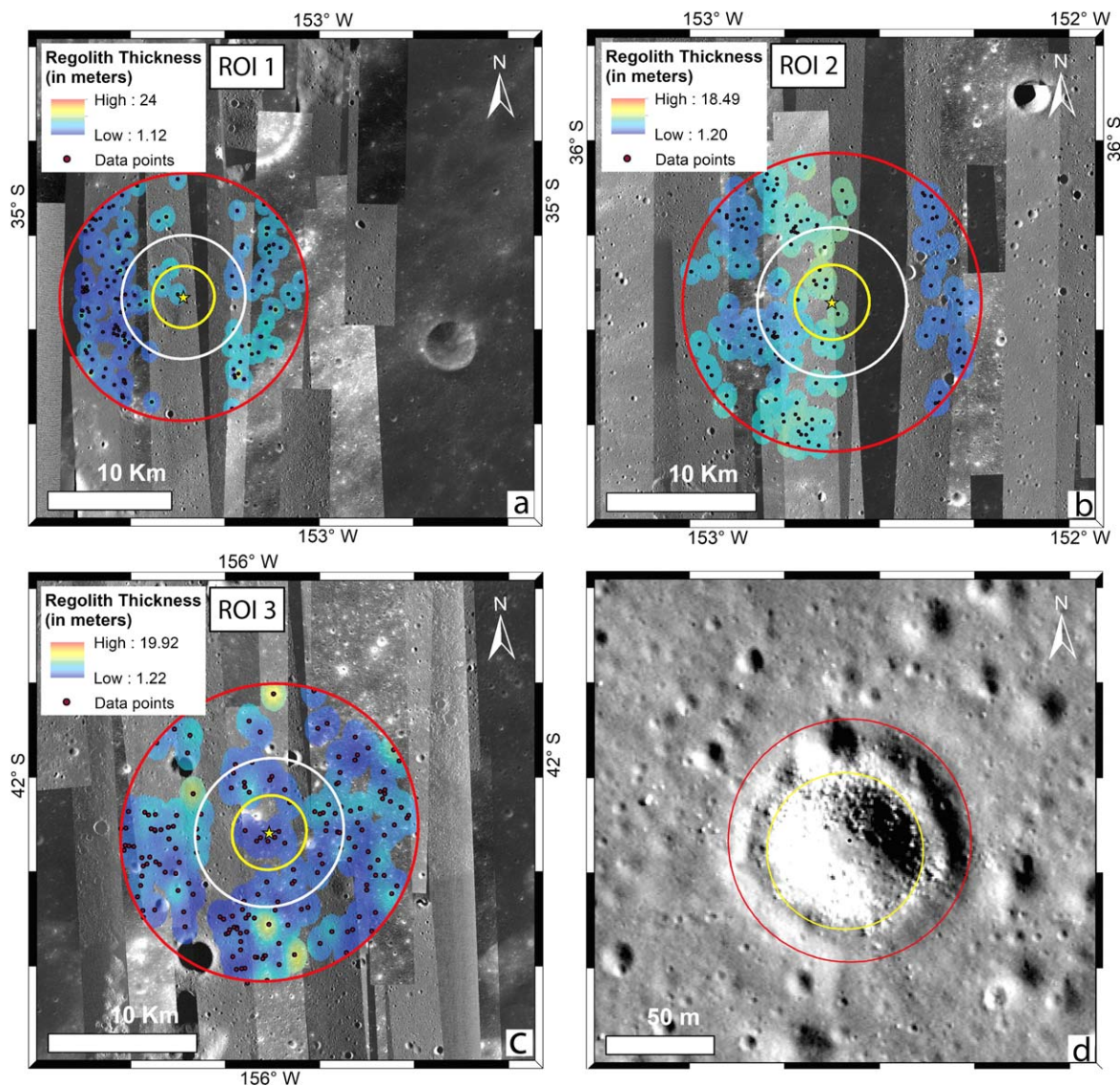


Figure 10. Maps of regolith thickness estimations for each ROI ((a), (b), and (c)) using Quaide & Oberbeck (1968). The data were derived by measuring the diameter of the inner and outer rim of CCs (d) using LROC NAC 1 m pixel⁻¹ data and applying the kriging technique to interpolate the results to the larger area. Points mark the measured values. The circles indicate exploration zones of 2.5, 5, and 10 km from the proposed landing site (yellow star). LROC NAC coverage as of 2018 February is overlaid over Kaguya TC data. The maps are in Lambert azimuthal equal-area projection, centered at -152.0°W , -35.8°S .

5.2.2.1. Central Apollo Mare Province

Within the central mare province where ROI 1 and ROI 2 are situated, we interpret a subsurface stratigraphy or sequence of impact events (Figure 12(a)) based on our observations. The upper part of the stratigraphy consists of a layer of fine-grained regolith, ranging from 1.1 to 24 m in ROI 1 and 18.5 m in ROI 2. This thickness is in line with the general understanding of regolith thickness, which is estimated to be around 20 m (Fa et al. 2015). The upper regolith layer becomes thicker toward the high-albedo Copernican ejecta rays that overlay the mare deposit (Figures 10(a) and (b)).

We have observed a mixed zone within this upper regolith layer, where the fine-grained regolith and HCP mafic material (depicted in yellow in Figure 11(a)) are exposed by small, fresh impact craters. These craters have excavated material between approximately 5.9 m and the maximum estimated regolith thickness.

The next layer in the stratigraphy is the mare deposit, which reaches a maximum depth of over 380 m. However, in the case

of “Crater 1,” instead of encountering impact melt or feldspathic material, mare materials have been excavated. Additionally, the ejecta from a large, unnamed, Copernican-aged crater overlaying Resnik crater in the northeastern part of the central mare province has exposed a feldspathic lithology known as the *NpNbh* unit (Figure 7).

Underlying the mare layer, we expect to find Imbrian ejecta layers from surrounding larger craters such as Dryden crater (3.69 billion yr; Upper Imbrian, according to Ivanov et al. 2018) and Borman V crater (Lower Imbrian). However, we cannot distinguish their ejecta deposits overlaying the mare deposit.

Beneath the *Ic* ejecta deposits, we anticipate the presence of light plains material. These light plains do not overlap stratigraphically with Dryden and Borman V craters, suggesting that these Imbrian large craters formed after the deposition of the light plains. The light plains may originate from the Orientale and Imbrium basin-forming events.

The subsequent layer in the stratigraphy should consist of ejecta deposits from various nearby Nectarian large craters,

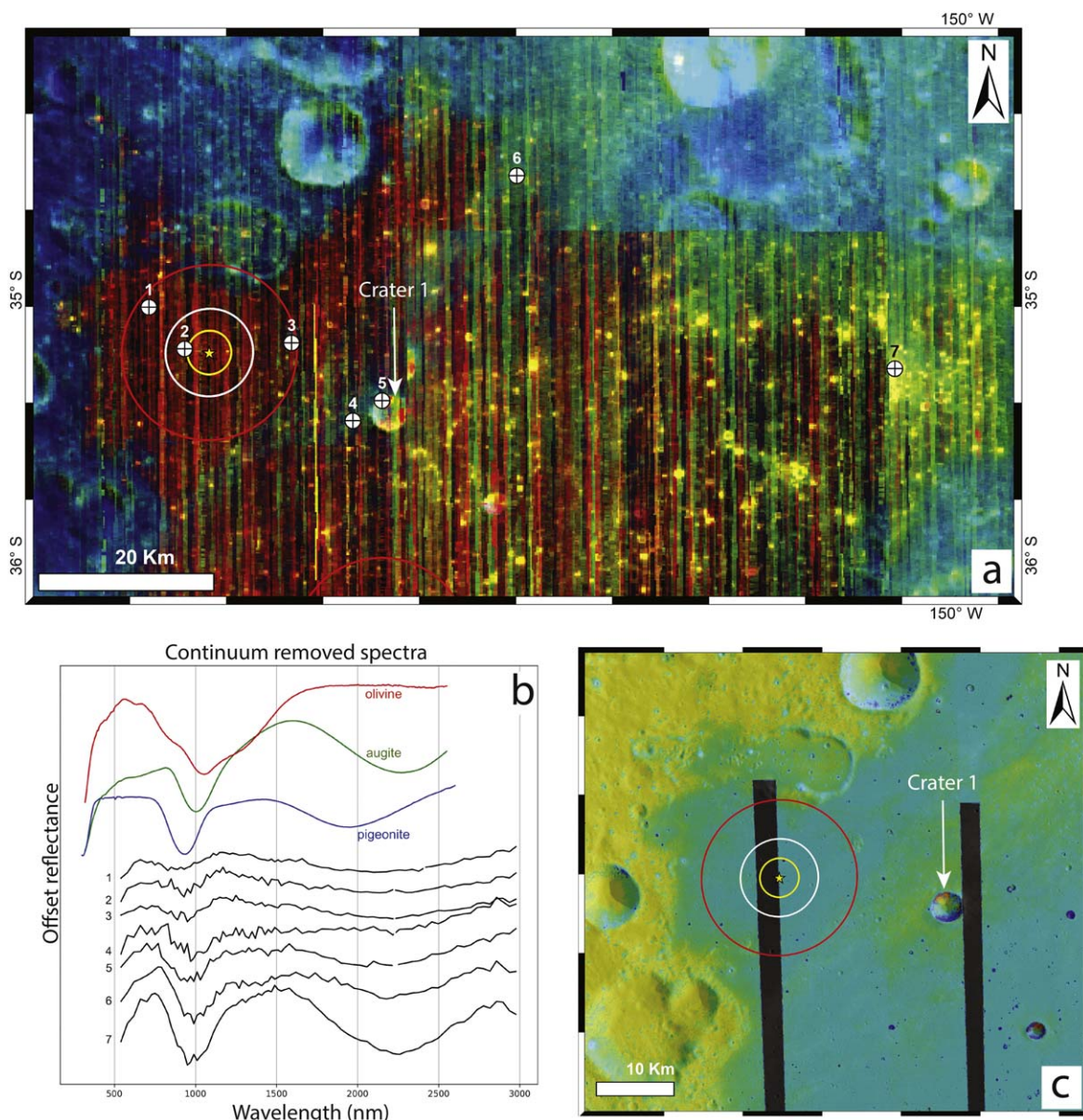


Figure 11. Chandrayaan M³ pyroxene spectral map and Kaguya MI overlaid on the LROC WAC mosaic showing the central mare province region in the Apollo basin. No distinct lava flows can be identified. (a) Chandrayaan M³ pyroxene spectral map showing the overview of the central mare province in the Apollo basin. (b) M³ spectra from seven key locations (indicated in panel (a)) compared with PDS spectral library data. Red: mature mare material; yellow: “fresh,” immature mare deposit; blue: feldspathic material. The ejecta of the large, unnamed Copernican-aged crater overlaying Resnik crater is a prominent feature even on spectral data. This ejecta deposit superposes “Crater 1” (marked with a white arrow in Figure 11) in the northeast–southwest direction (blue; number 4). Crater 1 is 4491 m in diameter with a calculated excavation depth of 377 m (Huang et al. 2018). Crater 1 might indicate exhumation of fresh mare material (yellow; number 5) similar to the small, fresh craters (numbers 2 and 7). (c) Kaguya MI spectral ratio map exhibiting the central mare province (light blue) and basin material (yellow) in the Apollo basin. The maps are in Lambert azimuthal equal-area projection, centered at -152.0°W , -35.8°S . M³ image numbers: M3G20090718T054612, M3G20090718T014252, M3G20090717T211502, M3G20090717T171142, M3G20090717T124352, M3G20090717T084032, M3G20090717T041548, M3G20090717T000932.

including Onizuka, Resnik, Jarvis, and Oppenheimer craters. The relative stratigraphy of these subdued and degraded craters is not clear without detailed analysis, such as AMA analysis, but they clearly formed before the formation of the mare deposit.

Finally, at the bottom of the stratigraphy, we expect to find the impact melts and breccias of the Apollo and SPA basins.

These proposed stratigraphies provide insight into the subsurface composition and sequence of impact events within the central mare province of the Apollo basin. However, further analysis and investigations, including in situ sampling and analysis, are necessary to validate and refine this proposed stratigraphy.

5.2.2.2. Southern Apollo Mare Province

In the southern mare province, Figure 12(b) presents a proposed subsurface stratigraphy. The upper part of the stratigraphy consists of a layer of fine-grained regolith, ranging from 1.2 to 19.9 m at ROI 3. The thickness of the upper regolith layer increases toward the center of the mare province, away from the outer rim of the Apollo basin. This accumulation of ejecta deposits on top of the mare is evident, with the ejecta of the Copernican Chaffee S crater serving as an example.

Similar to the central mare province, there is a mixed zone within the upper regolith layer, where the fine-grained regolith and HCP mafic material (depicted in yellow in Figure 11(a))

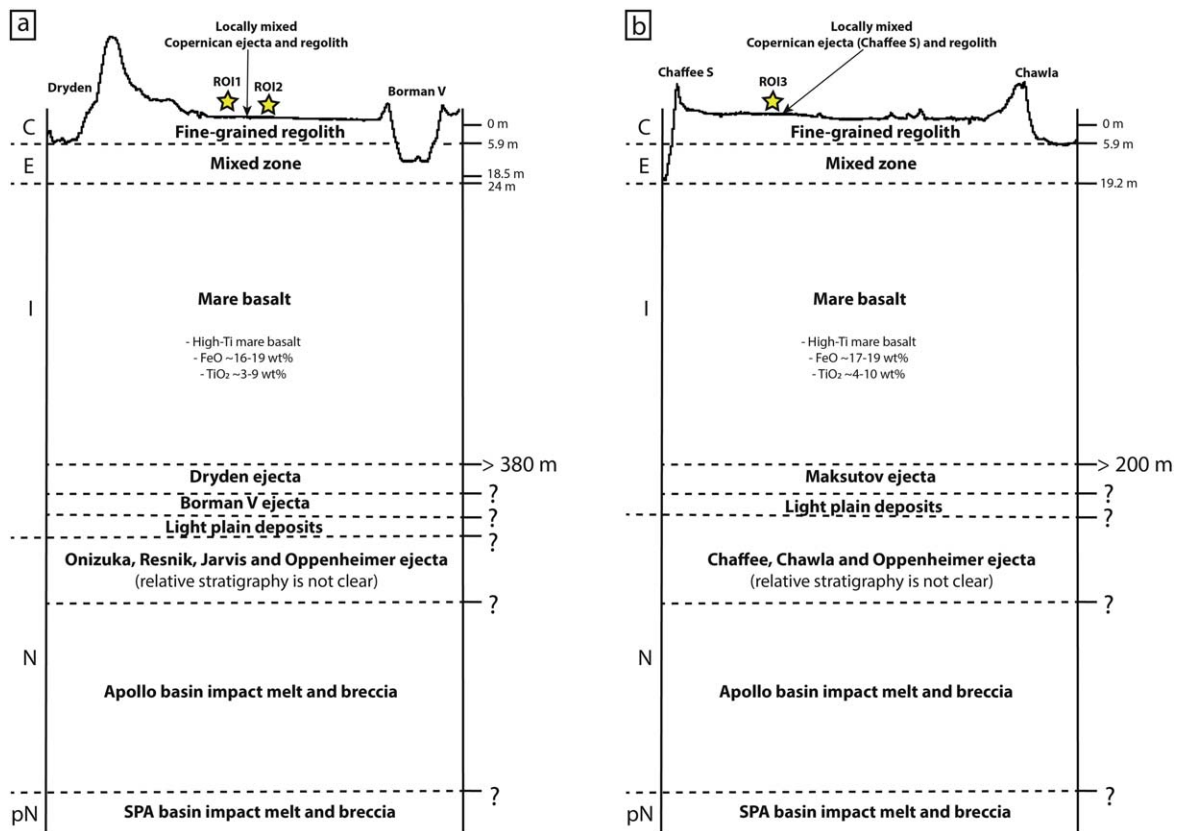


Figure 12. Based on this study, a proposed theoretical subsurface stratigraphy in the central (a) and southern (b) mare provinces.

are excavated by small, fresh impact craters. This mixed zone extends from approximately 5.9 m to the maximum estimated regolith thickness.

The next layer in the stratigraphy is the mare material, which, based on the estimated excavation depths of the largest crater, is at least ~ 200 m thick. Notably, there are no large craters overlaying the mare deposit that exhibit different mineralogical compositions.

Beneath the mare deposit, it is expected that the older impact melt and breccia from Maksutov crater (3.71 billion yr; Upper Imbrian according to Ivanov et al. 2018) should be located. However, Maksutov crater is situated outside of the Apollo basin, so the ejecta layer within the Apollo basin must be relatively thin, on the scale of centimeters.

The subsequent possible strata should be composed of the light plains deposits, which do not overlie Maksutov crater and must be older than it. Beneath the Imbrian ejecta materials, impact breccia from various nearby Nectarian large craters, such as Chaffee, Oppenheimer, and Chawla craters, are anticipated. However, the relative stratigraphy of these craters remains ambiguous. At the bottom of the stratigraphy, the impact melts and breccias from the SPA and Apollo basins are expected to be present.

It is important to note that this proposed subsurface stratigraphy is based on available data and interpretations. Further investigations and analysis, including in situ sampling and analysis, are necessary to validate and refine this proposed stratigraphy within the southern mare province of the Apollo basin.

5.2.3. ISRU Potential

Based on our findings, the Apollo basin within the SPA basin exhibits some of the highest FeO and TiO₂ contents.

These high abundances are associated with the Imbrian mare deposits, as illustrated in Figures 13 and 14, and supported by data provided in Tables 5 and 6.

Among the three ROIs, ROI 2 displays both the highest average and maximum FeO and TiO₂ contents. This suggests a significant presence of Fe and Ti in the mare deposits within ROI 2. On the other hand, ROI 1 has the lowest average and minimum FeO and TiO₂ values among all the ROIs but still exhibits relatively high FeO abundances.

These results highlight the variation in FeO and TiO₂ abundances within different regions of the Apollo basin. The high FeO and TiO₂ contents are characteristic of the Imbrian mare deposits found within the basin. The variations observed among the ROIs provide insights into the compositional diversity within the basin and contribute to our understanding of the lunar volcanism in this region.

6. Discussion

In this section, we discuss the open science questions and how these could be addressed by two robotic exploration mission scenarios with (1) lander and rover assets with a dedicated payload suite and (2) the same architecture with additional sample return capability. The following science objectives could be addressed by a robotic exploration mission at all ROIs.

1. Determine the age of the Apollo and SPA basins. Performing in situ detailed geochemical, isotopic, and petrologic analysis of lunar materials with additional sample return capability would allow us to advance our understanding of the bombardment history of the Moon.

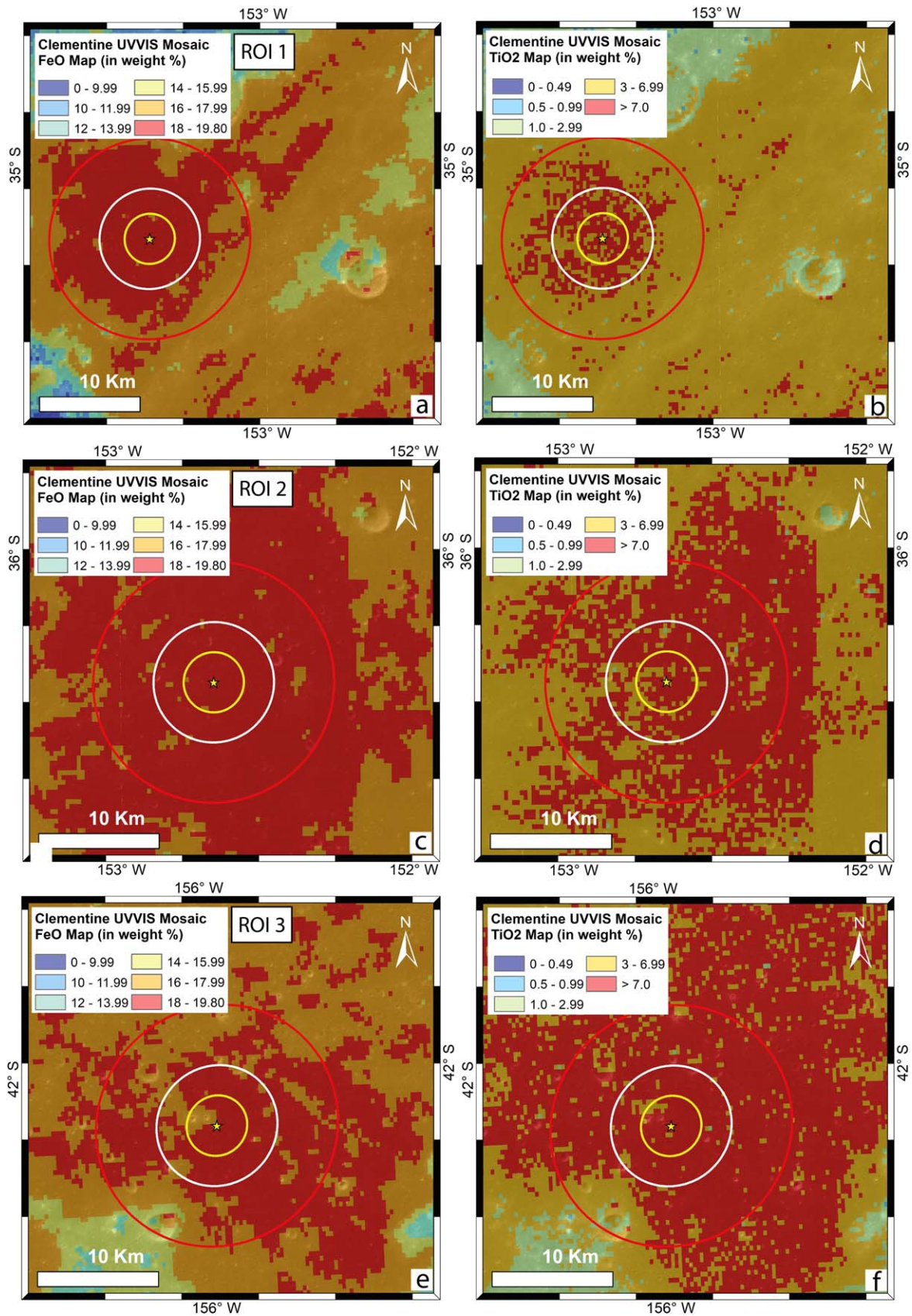


Figure 13. FeO and TiO₂ contents derived from Clementine 400 m pixel⁻¹ data overlaid on the Kaguya TC image. (a)–(b), (c)–(d), (e)–(f) FeO and TiO₂ contents of ROIs 1, 2, and 3, respectively. Lambert azimuthal equal-area projection, centered at -152.0°W , -35.8°S .

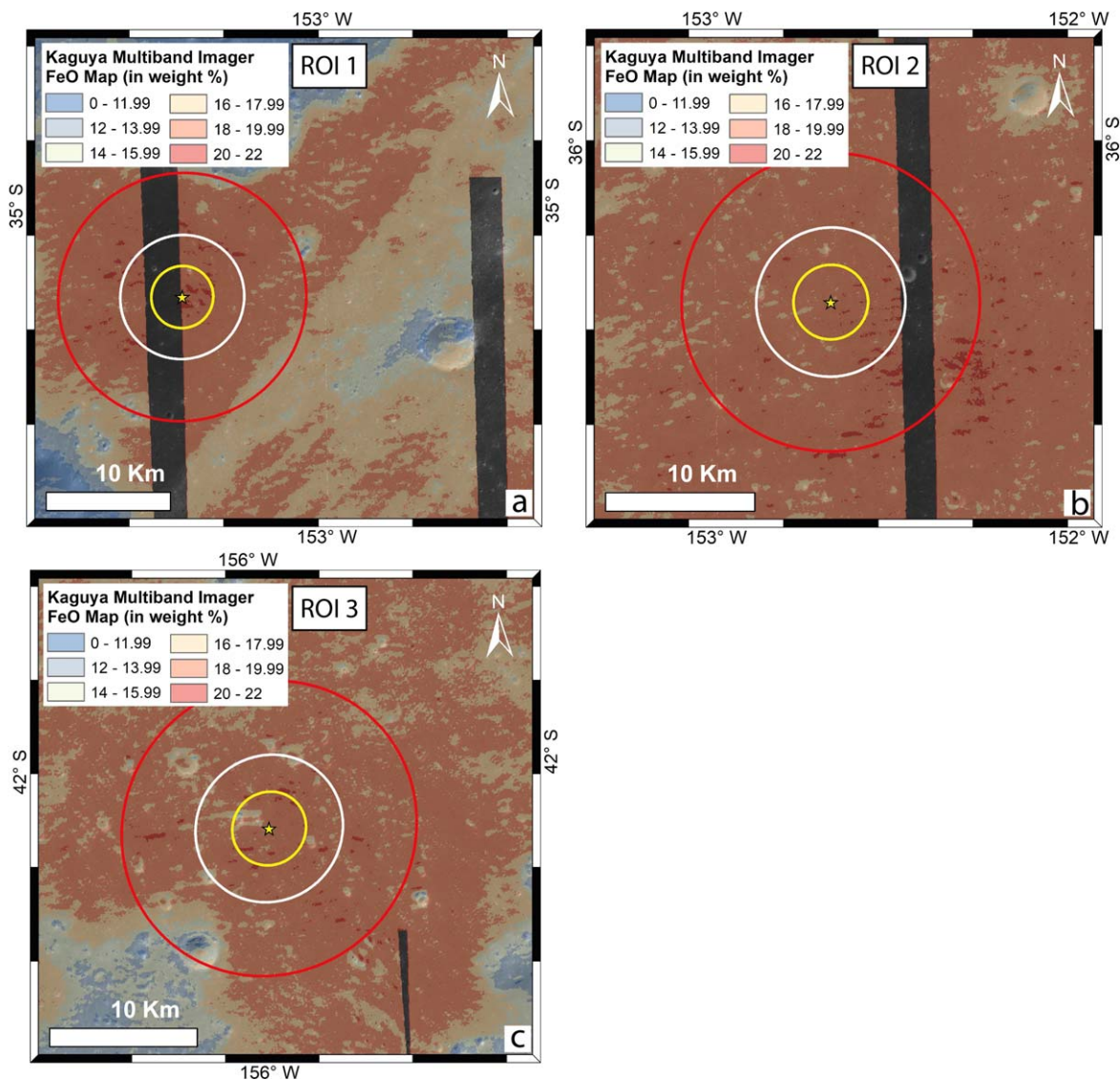


Figure 14. FeO abundances of mare deposits derived from Kaguya MI 60 m pixel⁻¹ data. Continuous stripes indicate no data. Lambert azimuthal equal-area projection, centered at -152.0°W, -35.8°S.

Table 5

FeO and TiO₂ Weight Percent of Mare Deposits Based on 400 m pixel⁻¹ Clementine Data

	ROI 1		ROI 2		ROI 3	
	FeO	TiO ₂	FeO	TiO ₂	FeO	TiO ₂
Min. wt%	16.15	3.51	17.65	4.82	17.39	4.05
Max. wt%	18.58	7.74	18.80	8.77	18.58	9.59
Average wt%	17.90	6.35	18.33	7.18	18.18	8.09
STDV	0.59	1.01	0.26	0.82	0.27	0.9

Table 6

FeO Weight Percent of Mare Deposits Based on Kaguya MI 60 m pixel⁻¹ Global Data Set

	ROI 1	ROI 2	ROI 3
Min.	14.09	16.59	17.41
Max.	20.54	20.15	20.39
Average	18.41	18.78	18.90
STDV	1.2	0.71	0.71

2. Determine the composition, age, and diversity of mare basalts on the farside of the Moon. A detailed compositional analysis of the lunar surface materials, particularly the mare deposits, could help to better understand their mineralogy, elemental composition, and variations in FeO and TiO₂ abundances. This analysis would provide insights into the magmatic evolution of the Apollo basin and the farside of the Moon.

3. Characterize the diversity and origin of rocks related to various geologic units. The investigation of the subsurface stratigraphy, including the layers of regolith, mare deposits, impact melt, and breccias, would contribute to our understanding of the formation and deposition of different units, the potential presence of older geologic materials beneath the Imbrian mare deposits, and the geologic evolution of the Apollo basin.

4. Characterize small impact craters at various degradation states and impact gardening processes in the Apollo

basin. By studying the distribution, morphology, and ages of craters within the ROIs, the mission can help unravel the recent impact history of the Apollo basin. This analysis would shed light on the chronology of recent impact events, the morphology of secondary craters, and the effects of cratering processes on the lunar surface.

5. Determine the thickness of the lunar crust, mantle, and core beneath the Apollo basin. Investigating the interior structure could reveal the physical and thermal evolution of the Moon, especially focusing on the early magma ocean history and thermal asymmetries of the nearside and farside of the Moon.
6. Determine the thickness, physical properties, and chemical composition of the regolith and megaregolith in the Apollo basin. A robotic mission can study the characteristics of the regolith, including its grain size distribution, physical properties, composition, and thermal behavior. These investigations would contribute to our understanding of regolith processes, such as impact gardening and regolith maturity, and provide valuable data for future lunar surface operations and resource utilization.

To maximize the science return, a carefully selected payload package for both the rover and lander can provide valuable data and address various scientific goals. Here is a breakdown for a proposed payload suite for the rover and lander, along with the potential scientific objectives they can address.

Rover Payload Suite.

1. *Panorama camera.* Provides oblique color images with stereo capability at gigapixel resolution, enabling panoramic visualization and detailed examination of geologic features of interest. This helps in characterizing the surface morphology, geological structures, and spatial relationships between different features.
2. *Close-up imager.* Captures high-resolution, color close-up images of rocks and regolith, allowing for detailed examination of their textures, mineralogy, and geological context. This supports the characterization of specific rock types, understanding their formation processes, and identifying potential targets for sample collection.
3. *Ground-penetrating radar (GPR).* Enables the observation of lateral and vertical subsurface structures by sending electromagnetic waves into the ground and analyzing the reflected signals. GPR helps in mapping subsurface layers, detecting buried structures, and studying the regolith's thickness, layering, and potential geological interfaces.
4. *Laser-induced breakdown spectrometer (LIBS).* Performs in situ qualitative and quantitative elemental analyses by using laser pulses to vaporize small portions of the surface material and analyze the emitted light. LIBS aids in determining the elemental composition of rocks, regolith, and potential mineralogical variations across different locations.
5. *Near and thermal infrared spectrometer.* Provides measurements of the reflectance and thermal emission of the lunar surface at different wavelengths. This helps in determining the mineralogical composition, identifying specific minerals, and studying the thermophysical properties of the surface, including temperature variations and thermal conductivity.

Lander Payload Suite.

1. *Passive and active seismology package.* Includes both passive and active seismometers to study lunar seismic activity. This package enables the characterization of moonquakes, impact-induced vibrations, and other seismic events, helping to understand the Moon's internal structure, crustal thickness, and potential tectonic activity.
2. *Heat flow experiment.* Measures the thermal gradient and heat flux from the lunar surface to provide insights into the Moon's thermal history and heat transfer processes. This experiment aids in understanding the thermal properties of the regolith, the thermal conductivity of the subsurface, and the overall heat flow from the interior.
3. *Drill.* Allows for the collection of subsurface samples, helping to characterize the subsurface stratigraphy and the structure of the megaregolith and potentially uncovering materials from different geological epochs. The drill provides access to deeper layers and helps in understanding the vertical variations in composition and geologic history.
4. *ISRU demonstration package.* Demonstrates the extraction and utilization of lunar resources and explores technologies and processes for resource extraction, refining, and utilization, paving the way for sustainable lunar operations.

The National Research Council (2007) goals that can be addressed by the proposed instruments are given in Table 7. These goals include objectives such as understanding lunar geology and the history of the Moon, studying the lunar interior and its structure, characterizing lunar resources, and enabling future human exploration and habitation.

By combining the capabilities of the rover and lander payloads, this mission architecture provides a comprehensive suite of instruments to address a wide range of scientific objectives, contributing to our understanding of the Moon's bombardment history, regolith processes, internal structure, volcanic evolution, and resources.

The National Research Council (2007) goals that could be addressed by a robotic exploration mission with lander and rover capability at the candidate landing sites in the Apollo basin are evaluated in Figure 15. Altogether, 12 plus 9 scientific goals from the National Research Council (2007) report could be or may be addressed, respectively. Science questions and goals from Campaign 5 of the European Space Agency's Strategy for Science at the Moon (European Space Agency 2019a) could be covered in the Apollo basin by a robotic exploration mission scenario.

With sample return capability, additional National Research Council (2007) goals could be addressed (Figure 16). Altogether, we identified 19 plus 5 scientific goals from the National Research Council (2007) that could be or may be addressed, respectively. Campaigns 1 and 5 of the European Space Agency's Strategy for Science at the Moon (European Space Agency 2019a) could be targeted by a sample return mission to the Apollo basin. Almost all National Research Council (2007) concepts would be addressed, seven more goals than without sample return capability.

Determining the duration of the lunar basin-forming epoch and calibrating the lunar chronology are high priorities in the

Table 7
National Research Council (2007) Goals Addressed or Possibly Addressed with the Proposed Instruments

	Panorama Camera	GPR	LIBS	NIR/TIR	Close-up Imager	Seismology Package	Heat Flow	Drill+NIR Camera
National Research Council (2007)	1e, 3e, 5a, 6a, 6b, 6c, 7b, 7c, 7d	1e, 3e, 6a, 6c, 6d, 7b, 7c	1b, 3a, 3b, 3c, 5a, 5b, 6a, 7d	3a, 3c, 5a, 6a, 6d, 7b, 7c, 7d	5a, 6a, 7b, 7d	2a, 2b, 2c, 3c, 3d, 3e, 6b	2d	1d, 3e, 6d, 7b, 7c, 7d

NRC Concept/ Goal	a	b	c	d	e
1. Bombardment history of the inner solar system	Test cataclysm hypothesis	Age of South Pole-Aitken	Establish absolute chronology	Recent impact flux	Secondary craters
2. Structure and composition of lunar interior	Thickness/variability of lunar crust	Stratification of mantle	Size, composition, state of core	Thermal state of interior	N/A
3. Diversity of lunar crustal rocks	Differentiation products	Age, distribution, origin of rocks	Composition of lower crust	Complexity of lunar crust	Extent/structure of megaregolith
4. Lunar poles and volatiles	State and distribution of volatiles	Source of volatiles	Transport, alteration, loss, processes	Properties of polar regolith	Polar regolith and ancient solar environment
5. Lunar volcanism	Origin/variability of basalts	Age of mare basalts	Range/extent of pyroclastic deposits	Lunar volcanic flux	N/A
6. Impact processes	Melt sheet differentiation	Structure of multi-ring impact basins	Crater formation	Mixing of local and ejecta material	N/A
7. Regolith processes	Characterize ancient regolith	Physical properties of regolith	Regolith modification processes	Rare minerals in regolith	N/A

Addressed
 Not addressed
 May be addressed

Figure 15. National Research Council (2007) science concepts and goals assessed for a robotic exploration mission with rover and lander assets in the Apollo basin. The highest-ranked National Research Council (2007) science concepts and goals cannot be fully addressed without sample return capability.

NRC Concept/ Goal	a	b	c	d	e
1. Bombardment history of the inner solar system	Test cataclysm hypothesis	Age of South Pole-Aitken	Establish absolute chronology	Recent impact flux	Secondary craters
2. Structure and composition of lunar interior	Thickness/variability of lunar crust	Stratification of mantle	Size, composition, state of core	Thermal state of interior	N/A
3. Diversity of lunar crustal rocks	Differentiation products	Age, distribution, origin of rocks	Composition of lower crust	Complexity of lunar crust	Extent/structure of megaregolith
4. Lunar poles and volatiles	State and distribution of volatiles	Source of volatiles	Transport, alteration, loss, processes	Properties of polar regolith	Polar regolith and ancient solar environment
5. Lunar volcanism	Origin/variability of basalts	Age of mare basalts	Range/extent of pyroclastic deposits	Lunar volcanic flux	N/A
6. Impact processes	Melt sheet differentiation	Structure of multi-ring impact basins	Crater formation	Mixing of local and ejecta material	N/A
7. Regolith processes	Characterize ancient regolith	Physical properties of regolith	Regolith modification processes	Rare minerals in regolith	N/A

Addressed
 Not addressed
 May be addressed

Figure 16. National Research Council (2007) science concepts and goals in the case of a robotic exploration mission to the lunar surface with a rover and lander with sample return capability. The highest-ranked science concepts and goals can be achieved with sample return capability.

lunar science community. The minimum requirement to solve the impact bombardment history of the Earth–Moon system and recalibrate the lunar chronology curve might only be possible by returning samples from several key geologic

features. Collecting impact melt-bearing samples could help to constrain the age of the Apollo basin, one of the youngest impact basins within the SPA basin, and possibly the age of SPA as well.

Additionally, the Apollo basin offers the opportunity to sample previously unsampled geochemical terrains within the SPA basin. This inner peak-ring basin formed at the boundary of SPA and the anorthositic highlands provides a cross section to constrain magma ocean crystallization processes, impact melt sheet differentiation, and volcanic processes on the farside of the Moon. Sampling the lunar mare on the farside would provide a unique opportunity to constrain the volcanic processes, reveal the difference in crustal and thermal evolution, and better understand the formation of the nearside and farside dichotomy boundary.

ESA's technology development, the European Large Logistics Lander (the EL3 lander, named Argonaut), will be supporting human exploration of the Moon throughout the end of the 2020s and the 2030s. Argonaut will be capable of delivering a combination of cargo items, scientific payloads, and small robotic assets (rovers) to the lunar surface, including retrieving samples from the surface and bringing them back to Earth for analysis (European Space Agency 2022). Sending cargo missions to the lunar surface every 2 or 3 yr could greatly enhance the diversity of samples collected from the Moon.

7. Conclusions

On the basis of the studied data, all ROIs fulfill the general hazard requirements, science interest, and ISRU potential for a robotic exploration mission, such as Chang'E-6 (Zeng et al. 2023), to the Apollo basin.

The main focus of this study is on the central and southern mare provinces in the Apollo basin. We selected three equally suitable ROIs based on terrain properties, science, and ISRU potentials. We highlighted exploration zones of 2.5, 5, and 10 km from each proposed landing site. Furthermore, we discussed each landing site in the context of key lunar science objectives from the National Research Council (2007) and Campaigns 1 and 5 of the European Space Agency's Strategy for Science at the Moon (European Space Agency 2019a), which could be addressed by robotic exploration missions with (1) lander and rover assets with a dedicated payload suite and (2) the same architecture with additional sample return capability. We conducted a series of geospatial data analyses. We investigated the topography, slopes, crater density, rock abundance, geology, and mineralogy and studied the subsurface stratigraphy of each ROI.

The studied ROIs are generally smooth, with average slopes of $<5^\circ$ at baselines of 7 m, with the exception of steeper slopes ($>25^\circ$) associated with fresh craters. High local rock abundances associated with these fresh craters still could allow for good traversability. The proposed ROIs reflect geologically complex areas, where mare deposits are covered by younger, Copernican-aged ejecta material with various thicknesses, compositions, and distributions. These ejecta materials have low FeO and TiO₂ contents representing nonmare deposits. The origin of that material could be reexcavated SPA and Apollo impact melt, which is the key sample type to address the lunar cataclysm hypothesis. In addition, the mare deposits have high ISRU potential with relatively high FeO and TiO₂ contents ranging from 16 to 20 wt% and 3 to 10 wt%, respectively. Additionally, all ROIs provide the opportunity to directly

sample material from the structure of the Apollo basin in the form of kipukas (ROIs 1 and 2), which are embayed hills by the mare deposits, or the outer basin rim of the Apollo basin could be sampled near a candidate landing site (ROI 3).

In situ observations with advanced rover and lander payload capabilities can help to address six of seven National Research Council concepts (1–3, 5–7), as well as Campaigns 1 and 5 of the European Space Agency's Strategy for Science at the Moon (European Space Agency 2019a). However, there is a great loss in science benefit without the sample return capability. A sample return mission could address 19 plus 5 scientific goals of the National Research Council (2007), while an in situ robotic exploration mission could aim to study 12 plus 9 scientific goals of the National Research Council (2007) in the Apollo basin, seven fewer goals than with samples brought back to our laboratories. To test the cataclysm hypothesis (Tera et al. 1974; Ryder 2002) and establish an accurate lunar chronology (concept 1), as well as study the diversity of lunar crustal rocks (concept 3), and lunar farside volcanism (concept 5; National Research Council 2007), a sample return mission scenario would be greatly beneficial. Thus, a successful Chang'E-6 sample return mission can achieve multiple science goals.

Acknowledgments

C.O. was funded by the Deutsche Forschungsgemeinschaft (SFB-TRR 170, subproject A3). C.O. is thankful for being hosted during the initial phase of this study at WWU in Münster. C.O. was additionally supported by the ESA Research Fellowship Program. I.T. was funded by the ESA Young Graduate Trainee Program. R.B. was supported by the ESA Research Fellowship Program. C.v.d.B. and H.H. are supported by German Aerospace Agency (DLR) grant No. 50 OW 2001 and as part of a project that has received funding from the European Union's Horizon 2020 research and innovation program under grant agreement No. 871149 (Europlanet 2024 RI, GMAP). The python code used to derive M3 data is available at <https://github.com/ines-torres/M3-data-processing>. This is TRR 170 Publication No. 198. The data presented in this study is available in the TRR170-DB Repository (doi:10.35003/PI5HHE).

Appendix Data Sets




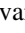

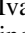
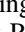
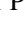

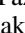
Data sets produced from this study are provided in this Appendix, which is organized into two directories, the name

Table A1
Data Sets and Software for This Study

Directory	Contents Description
geodatabase	Archived and compressed ArcGIS geodatabase (ApolloData.gdb.zip) containing rasters and shapefiles
tables	MS Excel (.xls) format spreadsheets (crater density, regolith thickness, FeO and TiO ₂ contents based on Clementine data, FeO content based on Kaguya data) for ROIs 1, 2, and 3

and content of which are described in Supporting Table A1. The data presented in this study will be available in the TRR170-DB Repository ([10.35003/PI5HHE](https://doi.org/10.35003/PI5HHE)).

ORCID iDs

Csilla Orgel  <https://orcid.org/0000-0001-7317-0092>
 Ines Torres  <https://orcid.org/0000-0003-4180-4905>
 Sebastien Besse  <https://orcid.org/0000-0002-1052-5439>
 Carolyn H. van der Bogert  <https://orcid.org/0000-0003-2882-7037>
 Mikhail A. Ivanov  <https://orcid.org/0000-0001-5696-8131>
 Harald Hiesinger  <https://orcid.org/0000-0001-7688-1965>
 Jan Hendrik Pasckert  <https://orcid.org/0000-0002-1338-5638>
 Mayssa El Yazidi  <https://orcid.org/0000-0002-1279-4173>
 Balazs Bradak  <https://orcid.org/0000-0003-4101-8621>
 Sebastian H. G. Walter  <https://orcid.org/0000-0003-2692-6162>

References

- Allen, C. C., Greenhagen, B. T., Donaldson Hanna, K. L., et al. 2012, *JGRE*, **117**, E00H28
- Allen, C. C. 2015, *LPSC*, **46**, 1140
- Allender, E. J., Orgel, C., Almeida, N. V., et al. 2019, *AdSpR*, **63**, 692
- Baker, D. M. H., & Head, J. W. 2015, *Icar*, **258**, 164
- Baker, D. M. H., Head, J. W., Fassett, C. I., et al. 2011, *Icar*, **214**, 377
- Bandfield, J. L., Ghent, R. R., Vasavada, A. R., et al. 2011, *JGRE*, **116**, E00H02
- Barker, M. K., Mazarico, E., Neumann, G. A., et al. 2016, *Icar*, **273**, 346
- Basilevsky, A. T., Abdrakhimov, A. M., Head, J. W., et al. 2015, *P&SS*, **117**, 385
- Basilevsky, A. T., Kreslavsky, M. A., Karachevtseva, I. P., et al. 2014, *P&SS*, **92**, 77
- Besse, S., sunshine, J., Staid, M., et al. 2013, *Icar*, **222**, 229
- Boardman, J. W., Pieters, C. M., Green, R. O., et al. 2011, *JGRE*, **116**, E00G14
- Borst, A. M., Foing, B. H., Davies, G. R., et al. 2012, *P&SS*, **68**, 76
- Cannon, K. M., Rampe, E., Malaret, E., et al. 2023, *LPSC*, **54**, 2130
- Chuang, F. C., Whitten, J. L., Domingue, D. L., et al. 2022, *LPSC*, **53**, 1449
- Clark, R. N., Pieters, C. M., Green, R. O., et al. 2011, *JGRE*, **116**, E00G16
- Crawford, I. A., Anand, M., Cockell, C. S., et al. 2012, *P&SS*, **74**, 3
- Djachkova, M. V., Litvak, M. L., Mitrofanov, I. G., et al. 2017, *SoSyR*, **51**, 185
- Ehresmann, M., Gabrielli, R. A., Herdrich, G., et al. 2017, *AcAau*, **134**, 189
- European Space Agency 2019a, ESA Strategy for Science at the Moon (Paris: ESA), https://sci.esa.int/documents/34161/35992/1567260389633-ESA_Strategy_for_Science_at_the_Moon.pdf
- European Space Agency 2019b, ESA Space Resources Strategy (Paris: ESA) https://sci.esa.int/documents/34161/35992/1567260390250-ESA_Space_Resources_Strategy.pdf
- European Space Agency 2022, Terrae Novae 2030+ Strategy Roadmap (Paris: ESA) https://esamultimedia.esa.int/docs/HRE/Terrae_Novae_2030+strategy_roadmap.pdf
- Fa, W., Liu, T., Zhu, M.-H., et al. 2014, *JGRE*, **119**, 1914
- Fa, W., Zhu, M.-H., Liu, T., et al. 2015, *GeoRL*, **42**, 10179
- Fassett, C. I. 2016, *JGRE*, **121**, 1900
- Flahaut, J., Carpenter, J., Williams, J.-P., et al. 2020, *P&SS*, **180**, 104750
- Fortezzo, C. M., Spudis, P. D., & Harrel, S. L. 2020, *LPSC*, **51**, 2760
- Fu, X.-H., Qiao, L., Zhang, J., et al. 2020, *RAA*, **20**, 8
- Gaddis, L., Staid, M. I., Tyburczy, J. A., et al. 2003, *Icar*, **161**, 262
- Garrick-Bethell, I., Miljkovic, K., Hiesinger, H., et al. 2020, *Icar*, **338**, 113430
- Garrick-Bethell, I., & Zuber, M. T. 2009, *Icar*, **204**, 399
- Gibson, K. E., & Jolliff, B. L. 2011, *LPSC*, **42**, 2326
- Green, R. O., Pieters, C., Mouroullis, P., et al. 2011, *JGRE*, **116**, E00G19
- Gruener, J. E., & Joosten, B. K. 2009, in Lunar Reconnaissance Orbiter Science Targeting Meeting, ed. S. J. Mackwell (Tempe, AZ: Arizona State Univ.), **58**
- Haruyama, J., Hara, S., Hioki, K., et al. 2012, *LPSC*, **43**, 1200
- Haruyama, J., Matsunaga, T., Ohtake, M., et al. 2008, *E&PS*, **60**, 243
- Haruyama, J., Ohtake, M., Matsunaga, T., et al. 2009, *Sci*, **323**, 905
- Head, J. W., & Wilson, L. 2020, *GeoRL*, **47**, E2020GL088334
- Hiesinger, H., van der Bogert, C. H., Pasckert, J. H., et al. 2012, *LPSC*, **43**, 2863
- Huang, J., Xiao, Z., Flahaut, J., et al. 2018, *JGRE*, **123**, 1684
- Hurwitz, D. M., & Kring, D. A. 2014, *JGRE*, **119**, 1110
- Ivanov, M. A., Hiesinger, H., van der Bogert, C. H., et al. 2018, *JGRE*, **123**, 2585
- Jawin, E. R., Valencia, S. N., Watkins, R. N., et al. 2019, *E&SS*, **6**, 2
- Jia, Y., Zou, Y., Ping, J., et al. 2018, *P&SS*, **162**, 207
- Jolliff, B., Petro, N., Moriarty, D., et al. 2021, *BAAS*, **53**, 290
- Jolliff, B., Watkins, R., Petro, N., et al. 2017, *LPSC*, **48**, 1326
- Jolliff, B. L., Gillis, J. J., Haskin, L. A., et al. 2000, *JGR*, **105**, 4197
- Jones, A. 2023, China's Yutu 2 Rover Still Going Strong After 4 Years on the Moon | Space.com: <https://www.space.com/china-yutu-2-rover-four-years-moon>
- Karachevtseva, I., Kozlova, N. A., Kokhanov, A. A., et al. 2017, *Icar*, **283**, 104
- Karachevtseva, I., Oberst, J., Scholten, F., et al. 2013, *P&SS*, **85**, 175
- Kato, M., Sasaki, S., & Takizawa, Y. 2010, *SSRv*, **154**, 3
- Keane, J. T., Tikoo, S. M., & Elliott, J. 2021, Endurance: Lunar South Pole–Aitken Basin Traverse and Sample Return Rover, Mission Concept Study Report for the 2023–2032 Planetary Science and Astrobiology Decadal Survey, NASA, <https://science.nasa.gov/wp-content/uploads/2023/11/endurance-spa-traverse-and-sample-return.pdf>
- Klima, R. L., Pieters, C. M., Boardman, J. W., et al. 2011, *JGRE*, **116**, E00G06
- Kramer, G. Y., Kring, D. A., Nahm, A. L., et al. 2013, *Icar*, **233**, 131
- Kring, D. A., & Durda, D. D. 2012, A Global Lunar Landing Site Study to Provide the Scientific Context for Exploration of the Moon, LPI Contribution No. 1694 (The Woodlands, TX: Lunar and Planetary Inst.), <https://www.lpi.usra.edu/exploration/CLSE-landing-site-study/>
- Lawrence, D. J., Feldman, W. C., Elphic, R. C., et al. 2002, *JGRE*, **107**, 5130
- Lunar Exploration Analysis Group 2016a, Lunar Exploration Roadmap—Opening the Gateway to the Solar System, <https://www.lpi.usra.edu/leag/roadmap/>
- Lunar Exploration Analysis Group 2016b, Lunar Human Exploration Strategic Knowledge Gap Special Action Team Review
- Lunar Exploration Analysis Group 2017, Advancing Science of the Moon: Report of the Specific Action Team, <https://www.lpi.usra.edu/leag/reports/ASM-SAT-Report-final.pdf>
- Lemelin, M., Li, S., Mazarico, E., et al. 2021, *PSJ*, **2**, 103
- Lemelin, M., Lucey, P. G., Gaddis, L. R., Hare, T., & Ohtake, M. 2016, *LPSC*, **47**, 2994
- Lucey, P. G., Blewett, D. T., & Jolliff, B. L. 2000, *JGR*, **105**, 20,297
- Lucey, P. G., Taylor, G. J., Hawke, B. R., et al. 1998a, *JGR*, **103**, 3701
- Lucey, P. G., Blewett, D. T., & Hawke, R. 1998b, *JGR*, **103**, 3679
- Martinet, M., Besse, S., Flahaut, J., et al. 2018, *JGRE*, **123**, 612
- Melosh, H. J. 1989, Impact Cratering: A Geologic Process (New York: Oxford Univ. Press)
- Melosh, H. J., Kendall, J., Horgan, B., et al. 2017, *Geo*, **45**, 1063
- Meyer, H. M., Denevi, B. W., Boyd, A. K., et al. 2016, *Icar*, **273**, 135
- Meyer, H. M., Denevi, B. W., Robinson, M. S., et al. 2020, *JGRE*, **125**, e06073
- Moriarty, D. P., Milla, M., Watkins, R. N., et al. 2022, *LPSC*, **53**, 2386
- Moriarty, D. P., & Pieters, C. M. 2014, *LPSC*, **45**, 2516
- Moriarty, D. P., & Pieters, C. M. 2016a, *LPSC*, **47**, 1735
- Moriarty, D. P., III, & Pieters, C. M. 2016b, *M&PS*, **51**, 207
- Moriarty, D. P., & Pieters, C. M. 2018, *JGRE*, **123**, 729
- Moriarty, D. P., III, Dygert, N., Valencia, S. N., et al. 2021a, *NatCo*, **12**, 4659
- Moriarty, D. P., III, Watkins, R. N., Valencia, S. N., et al. 2021b, *JGR*, **126**, e06589
- Moriarty, D. P., III, & Pieters, C. M. 2015, *GeoRL*, **42**, 7907
- National Research Council 2007, The Scientific Context for Exploration of the Moon—The National Academies Press (Washington, DC: The National Academies Press)
- Ohtake, M., Pieters, C. M., Isaacson, P. B., et al. 2013, *Icar*, **226**, 364
- Oliver, M. A., & Webster, R. 1990, *JGIS*, **4**, 313
- Orgel, C., Michael, G., Fassett, C. I., et al. 2018, *JGRE*, **123**, 748
- Pasckert, J. H., Hiesinger, H., & van der Bogert, C. H. 2018, *Icar*, **299**, 538
- Pieters, C. M., Boardman, J., Buratti, B., et al. 2009, *CSci*, **96**, 500, <https://www.jstor.org/stable/24105459>
- Pieters, C. M., Head, J. W., Gaddis, L., et al. 2001, *JGR*, **106**, 28001
- Poehler, C. M., van der Bogert, C. H., Hiesinger, H., et al. 2021, Annual Meeting of Planetary Geologic Mappers, **2610**, 7032
- Potter, R. W. K., Head, J. W., Guo, D., et al. 2018, *Icar*, **306**, 139
- Potts, N. J., Gullikson, A. L., Curran, N. M., et al. 2015, *AdSpR*, **55**, 1241
- Prieur, N. C., Rolf, T., Wünnemann, K., et al. 2018, *JGRE*, **123**, 1555
- Qiao, L., Zhu, P., Fang, G., et al. 2015, *Sci*, **347**, 1226
- Quaide, W. L., & Oberbeck, V. R. 1968, *JGR*, **73**, 5247
- Robinson, M. S., Brylow, S. M., Tschimmel, M., et al. 2010, *SSRv*, **150**, 81

- Ryder, G. 2002, *JGRE*, **107**, 5022
- Smith, D. E., Zuber, M. T., Jackson, G. B., et al. 2010, *SSRv*, **150**, 209
- Steenstra, E. S., Martin, D. J., McDonald, F. E., et al. 2016, *AdSpR*, **58**, 1050
- Stuart-Alexander, D. E. 1978, *Geologic Map of the Central Far Side of the Moon* MAP 1047, USGS
- Tera, F., Papanastassiou, D. A., & Wasserburg, G. J. 1974, *E&PSL*, **22**, 1
- Thiessen, F., Hiesinger, H., van der Bogert, C. H., et al. 2012, *LPSC*, **43**, 2060
- Torres, I., Orgel, C., Besse, S., et al. 2022, in Planetary Science Informatics and Data Analytics Conf. (Paris: ESA), J07, https://www.cosmos.esa.int/documents/6109777/8769248/PSIDA2022_Abstracts+%281%29_Part16.pdf/2729dd42-96d3-e4e6-c712-aed370eab39a?t=1652804621944
- Trang, D., Gillis-Davis, J., Williams, K., et al. 2010, *LPSC*, **41**, 2652
- van der Bogert, C. H., Hiesinger, H., Dundas, C. M., et al. 2017, *Icar*, **298**, 49
- van der Bogert, C. H., Hiesinger, H., Pretto, I., et al. 2021, *PSJ*, **2**, 84
- Vaughan, W. M., & Head, J. W. 2014, *P&SS*, **91**, 101
- Wang, Q., & Liu, J. 2016, *AcAau*, **127**, 678
- Whitten, J. L., & Head, J. W. 2015, *Icar*, **247**, 150
- Wieczorek, M. A., Neumann, G. A., Nimmo, F., et al. 2013, *Sci*, **339**, 671
- Wieczorek, M. A., & Phillips, R. J. 2000, *JGR*, **105**, 20417
- Wilhelms, D. E., Howard, K. A., & Wilshire, H. G. 1979, *Geologic Map of the South Side of the Moon* IMAF 1162, USGS
- Wilhelms, D. E., McCauley, J. F., & Trask, N. J. 1987, *The Geologic History of the Moon* Professional Paper 1348, USGS
- Wu, B., Li, F., Ye, L., et al. 2014, *E&PSL*, **405**, 257
- Wu, W., Li, C., Zuo, W., et al. 2019, *NatGe*, **12**, 222
- Yamamoto, S., Nakamura, R., Matsunaga, T., et al. 2012, *Icar*, **218**, 331
- Yingst, A., & Head, J. W. 1999, *JGR*, **104**, 18957
- Zeng, X., Liu, D., Chen, Y., et al. 2023, *NatAs*, **7**, 1188